



# Interfacial oxygen vacancies at $\text{Co}_3\text{O}_4\text{-CeO}_2$ heterointerfaces boost the catalytic reduction of NO by CO in the presence of $\text{O}_2$

Shaomian Liu<sup>a,b,1</sup>, Wenjuan Xue<sup>c,1</sup>, Yongjun Ji<sup>d,\*</sup>, Wenqing Xu<sup>a,\*</sup>, Wenxing Chen<sup>e,\*</sup>, Lihua Jia<sup>f</sup>, Tingyu Zhu<sup>a</sup>, Ziyi Zhong<sup>g,h</sup>, Guangwen Xu<sup>i</sup>, Donghai Mei<sup>c,j,\*\*</sup>, Fabing Su<sup>a,i,\*\*\*</sup>

<sup>a</sup> Institute of Process Engineering, Chinese Academy of Sciences, Beijing 100190, PR China

<sup>b</sup> School of Chemical Engineering, University of Chinese Academy of Sciences, 100049 Beijing, China

<sup>c</sup> School of Materials Science and Engineering, Tiangong University, Tianjin 300387, China

<sup>d</sup> School of Light Industry, Beijing Technology and Business University, Beijing 100048, China

<sup>e</sup> Energy & Catalysis Center, School of Materials Science and Engineering, Beijing Institute of Technology, Beijing 100081, China

<sup>f</sup> College of Chemistry and Chemical Engineering, Qiqihaer University, Qiqihaer 161006, Heilongjiang Province, China

<sup>g</sup> Department of Chemical Engineering, Guangdong Technion-Israel Institute of Technology (GTIT), 241 Daxue Road, Shantou 515063, China

<sup>h</sup> Technion-Israel Institute of Technology (IIT), Haifa 32000, Israel

<sup>i</sup> Institute of Industrial Chemistry and Energy Technology, Shenyang University of Chemical Technology, Shenyang 110142, China

<sup>j</sup> School of Environmental Science and Engineering, Tiangong University, Tianjin 300387, PR China

## ARTICLE INFO

### Keywords:

Ball milling  
Interfacial oxygen vacancies  
 $\text{Co}_3\text{O}_4\text{-CeO}_2$  composites  
CO-SCR  
 $\text{O}_2$ -containing conditions

## ABSTRACT

Simultaneously improving both  $\text{NO}_x$  conversion and  $\text{N}_2$  selectivity in the selective catalytic reduction of NO by CO (CO-SCR) under  $\text{O}_2$ -containing conditions is highly challenging because of the competitive reactions of  $\text{NO}_x$  and CO with  $\text{O}_2$ . Here, we demonstrate that the interfacial oxygen vacancies (IOVs) generated at the  $\text{Co}_3\text{O}_4\text{-CeO}_2$  heterointerfaces by ball-milling-induced strain can remarkably boost both  $\text{NO}_x$  conversion and  $\text{N}_2$  selectivity in the temperature range of 100–400 °C. The  $\text{Co}_3\text{O}_4\text{-CeO}_2\text{-IOV}$  catalyst achieved approximately 100%  $\text{NO}_x$  conversion and 100%  $\text{N}_2$  selectivity (200–350 °C, 1–5 vol%  $\text{O}_2$ , and 20,000  $\text{h}^{-1}$ ); even under 10 vol%  $\text{O}_2$ , it still showed good catalytic performance. The spectroscopy analysis and theoretical calculations reveal that compared with  $\text{O}_2$  activation, IOVs are more favorable for the rate-limiting step of NO adsorption and dissociation. This work provides an effective strategy to create IOVs within metal oxide composite catalysts using ball-milling-induced interfacial strain for improving CO-SCR performance.

## 1. Introduction

Ammonia selective catalytic reduction ( $\text{NH}_3\text{-SCR}$ ) technology has been widely used to control  $\text{NO}_x$  emission in automobile and factory exhaust gases [1,2]. However,  $\text{NH}_3$  as the reductant gas may lead to high operation costs, potential toxic risks, and catalyst poisoning from ammonium bisulfate [3]. Usually, these exhaust gases also contain CO, which can be used as a reductant gas instead of  $\text{NH}_3$  to selectively catalyze  $\text{NO}_x$  reduction to  $\text{N}_2$  (CO-SCR) [4,5], simultaneously eliminating two harmful gases,  $\text{NO}_x$  and CO. Owing to the low cost, a large number of transition metal oxides (TMOs) have been explored as CO-SCR catalysts, including  $\text{CuO}_x$  [6],  $\text{MnO}_x$  [7],  $\text{Co}_3\text{O}_4$  [8],  $\text{NiO}$  [9],

$\text{FeO}_x$  [10], and  $\text{CeO}_2$  [11], which exhibited excellent catalytic performance in the absence of  $\text{O}_2$ . However, the real exhaust gases often contain  $\text{O}_2$ , and meanwhile, CO and NO preferentially react with  $\text{O}_2$  to form  $\text{CO}_2$  and  $\text{NO}_2$  [12], resulting in poor NO conversion and  $\text{N}_2$  selectivity, especially at low temperatures.

Among the reported TMOs,  $\text{Co}_3\text{O}_4$  and  $\text{CeO}_2$ , with excellent redox properties, have aroused intensive research interest for CO-SCR [13–16]. Also, it has been proven that introducing surface oxygen vacancies (SOVs) in  $\text{Co}_3\text{O}_4$  and  $\text{CeO}_2$  as NO dissociating sites can effectively improve their catalytic performance. For example, the nonstoichiometric  $\text{CoO}_{1-x}$  catalysts containing SOVs achieved 100% NO conversion at 170 °C in the absence of  $\text{O}_2$  [8]; the Ni-doped  $\text{Fe/CeO}_2$

\* Corresponding authors.

\*\* Corresponding author at: School of Materials Science and Engineering, Tiangong University, Tianjin 300387, China.

\*\*\* Corresponding author at: Institute of Process Engineering, Chinese Academy of Sciences, Beijing 100190, PR China.

E-mail addresses: [yji@btbu.edu.cn](mailto:yji@btbu.edu.cn) (Y. Ji), [wqxu@ipe.ac.cn](mailto:wqxu@ipe.ac.cn) (W. Xu), [wxchen@bit.edu.cn](mailto>wxchen@bit.edu.cn) (W. Chen), [dhmei@tiangong.edu.cn](mailto:dhmei@tiangong.edu.cn) (D. Mei), [fbsu@ipe.ac.cn](mailto:fbsu@ipe.ac.cn) (F. Su).

<sup>1</sup> These authors contributed equally to this work.

catalyst with SOVs enhanced O<sub>2</sub> resistance and achieved 92% NO conversion at 150 °C in the presence of 0.5 vol% O<sub>2</sub> [17]; Cu-Ce-Fe-Co/TiO<sub>2</sub> achieved 63% NO conversion at 200 °C in the presence of 6 vol% O<sub>2</sub> because of its high concentration of SOVs and high oxygen mobility [7]; and the CoCeO<sub>x</sub> catalysts synthesized by calcining the precursor after grinding exhibited 26% NO conversion and 73% N<sub>2</sub> selectivity at 250 °C in the presence of 2 vol% O<sub>2</sub> [14]. However, owing to the significant excess electrons, SOVs as electron donors can competitively adsorb excessive O<sub>2</sub> on the single metal oxide catalyst under realistic environments (more than 2 vol% O<sub>2</sub>), lowering the NO conversion ( $\leq 85\%$ ) and N<sub>2</sub> selectivity ( $\leq 75\%$ ), and even causing the deactivation of catalysts [7, 14,17].

In recent years, interfacial oxygen vacancies (IOVs) generated at various metal oxide interfaces have attracted extensive attention in catalysis due to their unique properties different from the SOVs of single oxide catalysts [18]. It is revealed that IOVs have adjustable selective adsorption/desorption behaviors and longer lifetimes due to the synergistic effect of hetero-oxides on both sides of the interface [19]. Some composite catalysts with induced IOVs have shown good catalytic performance in photocatalysis [20], electrocatalysis [21], and thermal catalysis (toluene combustion [18], oxidative desulfurization [22], and water gas shift [23]). Inspired by these studies, it is expected that creating IOVs within the Co<sub>3</sub>O<sub>4</sub> and CeO<sub>2</sub> composite catalyst may boost its low-temperature catalytic performance in CO-SCR under real industrial conditions. However, to our knowledge, there has been no such report in the literature thus far.

Herein, we employ ball-milling-induced interfacial strain to generate IOVs at the Co<sub>3</sub>O<sub>4</sub>-CeO<sub>2</sub> complex heterointerfaces in the Co<sub>3</sub>O<sub>4</sub>-CeO<sub>2</sub>-IOV catalyst. When used as a CO-SCR catalyst in the presence of 5 vol% O<sub>2</sub>, Co<sub>3</sub>O<sub>4</sub>-CeO<sub>2</sub>-IOV exhibited 94% NO<sub>x</sub> conversion and 100% N<sub>2</sub> selectivity in the temperature range of 200–350 °C, superior to those of the most reported Co-/Ce-based catalysts. The *in situ* diffuse reflectance infrared Fourier transform spectroscopy (*in situ* DRIFTS) analysis and density functional theory (DFT) calculation reveal that the IOVs promote the adsorption and dissociation of NO, which is the rate-determining step of the CO-SCR reaction, especially compared with the activation of O<sub>2</sub>. This work demonstrates a facile approach to engineering the interface structure of catalysts for their better catalytic performance.

## 2. Experimental

### 2.1. Chemicals

All the chemical reagents used in this experiment were obtained from commercial sources and used without any other treatments, including cobalt nitrate hexahydrate (Co(NO<sub>3</sub>)<sub>2</sub>·6H<sub>2</sub>O, AR,  $\geq 99.5$  wt%, Maclean Biochemical Technology Co. Ltd.), cerium nitrate hexahydrate (Ce(NO<sub>3</sub>)<sub>3</sub>·6H<sub>2</sub>O, AR,  $\geq 99$  wt%, Aladdin Industrial Co. Ltd.), sodium carbonate (Na<sub>2</sub>CO<sub>3</sub>, AR,  $\geq 99.8$  wt%, Sinopharm Chemical Reagent Co. Ltd.), and potassium bromide (KBr, SP,  $\geq 99.8$  wt%, Beijing Yinglaike Technology Development Co. Ltd.). Deionized water was used in all the experiments.

### 2.2. Preparation of catalysts

**Co<sub>3</sub>O<sub>4</sub>-CeO<sub>2</sub> catalyst:** 27.51 g of Co(NO<sub>3</sub>)<sub>2</sub>·6H<sub>2</sub>O and 41.04 g of Ce(NO<sub>3</sub>)<sub>3</sub>·6H<sub>2</sub>O with an equal mole of Co and Ce were dissolved in 450 mL of deionized water, and the mixture was heated to 70 °C under vigorous stirring and maintained at this temperature for 10 min. Next, 150 mL of Na<sub>2</sub>CO<sub>3</sub> aqueous solution (1.25 M) was added to the above solution to form the slurry, which was further aged for 1 h at room temperature. Subsequently, the precipitant powder was collected and washed three times with deionized water and finally with ethanol one time. Later, the collected solid was dried at 100 °C for 6 h and calcined in air at 500 °C (5 °C min<sup>-1</sup>) for 5 h to obtain the Co<sub>3</sub>O<sub>4</sub>-CeO<sub>2</sub> catalyst.

**The Co<sub>3</sub>O<sub>4</sub>-CeO<sub>2</sub>-IOV catalyst:** 12.00 g of Co<sub>3</sub>O<sub>4</sub>-CeO<sub>2</sub> was ball-milled at room temperature with 180 g of zirconia balls (5 mm in diameter) in an agate vial using the Planet-Ball-Grinding machine (QM-3SPO4, Nanjing University instrument plant, China) at 580 rpm for 2 h. The obtained catalyst was denoted as Co<sub>3</sub>O<sub>4</sub>-CeO<sub>2</sub>-IOV.

**The Co<sub>3</sub>O<sub>4</sub>-CeO<sub>2</sub>-IOV-C catalyst:** 6.00 g of the above Co<sub>3</sub>O<sub>4</sub>-CeO<sub>2</sub>-IOV sample was calcined in air at 500 °C (5 °C min<sup>-1</sup>) for 5 h to obtain the Co<sub>3</sub>O<sub>4</sub>-CeO<sub>2</sub>-IOV-C catalyst for comparison purpose.

The content of Co<sub>3</sub>O<sub>4</sub> and CeO<sub>2</sub> in the above three catalysts was approximately 31.8 wt% and 68.2 wt%, respectively, calculated based on the feeding amounts of the precursors in the synthesis.

**The Co<sub>3</sub>O<sub>4</sub>+CeO<sub>2</sub> catalyst:** Co<sub>3</sub>O<sub>4</sub> and CeO<sub>2</sub> were prepared separately by the same method as the Co<sub>3</sub>O<sub>4</sub>-CeO<sub>2</sub> catalyst using one individual metal precursor each time, and 2.28 g of Co<sub>3</sub>O<sub>4</sub> and 4.88 g of CeO<sub>2</sub> were then physically mixed through grinding in a mortar for 5 min (denoted as Co<sub>3</sub>O<sub>4</sub>+CeO<sub>2</sub>).

**The Co<sub>3</sub>O<sub>4</sub>-M+CeO<sub>2</sub>-M catalyst:** the Co<sub>3</sub>O<sub>4</sub>-M and CeO<sub>2</sub>-M samples (M represents ball milling) were prepared separately by the same method as the Co<sub>3</sub>O<sub>4</sub>-CeO<sub>2</sub>-IOV catalyst by adding only one individual metal precursor each time, and 2.28 g of Co<sub>3</sub>O<sub>4</sub>-M and 4.88 g of CeO<sub>2</sub>-M were physically mixed through grinding in a mortar for 5 min (denoted as Co<sub>3</sub>O<sub>4</sub>-M+CeO<sub>2</sub>-M).

### 2.3. Characterization

The microscopic features of the catalyst were observed by field-emission scanning electron microscopy (SEM) (JSM-7001 F, JEOL, Tokyo, Japan) and transmission electron microscopy (TEM) (JEM-2010 F, JEOL, Tokyo, Japan) with energy-dispersive spectroscopy (EDS). The crystalline phases in the catalysts were characterized by X-ray diffraction (XRD) using Cu K $\alpha$  radiation ( $k = 1.5418$  Å) at 40 kV and 40 mA from 10.0 to 90.0° (PANalytica X'Pert PRO MPD). The crystallite sizes ( $D_{\beta}$ ) of all catalysts were calculated using the Debye-Scherrer equation ( $D_{\beta} = K\lambda/\beta \cos\theta$ ). Hydrogen temperature-programmed reduction (H<sub>2</sub>-TPR) was carried out on an automated chemisorption analyzer (ChemBET pulsar TPR/TPD, Quantachrome). Temperature-programmed desorption of O<sub>2</sub> (O<sub>2</sub>-TPD) was performed using a Quantachrome Autosorb Iq instrument (see the detailed description in SI). The metal contents in the catalysts were measured by inductively coupled plasma-optical emission spectroscopy (ICP-OES, Perkin-Elmer Optima 5300DV, America). The particle size distribution (PSD) was measured by a laser particle size analyzer (BT-9300Z, Bettersize Instruments Ltd., China). The specific surface area was determined according to the Brunauer-Emmett-Teller (BET) method (NOVA 3200e, Quantachrome) by nitrogen physisorption at -196 °C. The pore size distribution was calculated with the Barrett-Joyner-Halenda (BJH) method using the adsorption isotherm branch. The surface chemical composition was determined by X-ray photoelectron spectroscopy (XPS) (Model VG ESCALAB 250 spectrometer, Thermo Electron, U.K.) using nonmonochromatized Al K $\alpha$  X-ray radiation ( $h\nu = 1486.6$  eV). Raman spectroscopic analysis was performed on an InVia Reflex (England) with a wavelength of 532 nm. The UV-Vis DRS experiments were performed on a UV-Vis spectrophotometer (Hitachi U-4100) with the integration sphere diffuse reflectance attachment. X-band electron paramagnetic resonance (EPR) spectra were recorded on a JEOL JES-RE2X electron spin resonance spectrometer at 70 K (BRUKER E500). The g values were calibrated using 2, 2-diphenyl-1-picrylhydrazil (g'/2.0036) as a standard. A Nicolet 6700 Fourier transform-infrared spectrophotometer (Thermo Fisher, Germany) was used to conduct FT-IR analyses. *In situ* DRIFTS experiments were performed to test the adsorption of NO and CO on catalysts. First, the catalyst sample and KBr were physically mixed in a weight ratio of 1:10, and pretreated in the flow of pure N<sub>2</sub> (100 mL min<sup>-1</sup>) at 400 °C for 1 h, then cooled down to the test temperature. The background spectra were collected during the cooling procedure in the atmosphere of pure N<sub>2</sub> (100 mL min<sup>-1</sup>) and subtracted from the corresponding spectra. During the DRIFTS tests, the adopted conditions were

as follows: 1000 ppm NO + 5 vol% O<sub>2</sub>, or / and 2000 ppm CO, N<sub>2</sub> as the balance gas, and the total flow rate at 100 mL min<sup>-1</sup>. All these spectra were collected by accumulating 32 scans in the range of 600–4000 cm<sup>-1</sup> at a resolution of 4 cm<sup>-1</sup> as a function of time. The XAFS spectra (O K-edge) were collected at station 1W1B in the Beijing Synchrotron Radiation Facility (BSRF, operated at 2.5 GeV with a maximum current of 250 mA). The catalysts were deposited onto a piece of double-sided carbon tape for X-ray spectroscopy analysis. The extended X-ray absorption fine structure (EXAFS) spectra data were collected at BL14W1 station in Shanghai Synchrotron Radiation Facility (SSRF, operated at 3.5 GeV with a maximum current of 250 mA), respectively (see the detailed description in SI).

## 2.4. Catalytic measurement

The CO-SCR reaction was conducted in a fixed-bed quartz tubular reactor (inner diameter: 8 mm) with a thermocouple at its center. The catalysts were pre-treated in a CO/N<sub>2</sub> (2000 ppm CO and N<sub>2</sub> as balance gas) gas mixture at a flow of 1 L min<sup>-1</sup> at 200 °C for 1 h before each test. The catalytic activity of each 20–40 mesh catalyst (3 mL) was examined, and the experiments were performed at 100–400 °C. The inlet gas comprised of NO (1000 ppm), CO (2000 ppm), O<sub>2</sub> (5 vol%), SO<sub>2</sub> (in use 50 ppm), H<sub>2</sub>O (in use 10 vol%), and N<sub>2</sub> (the balance). Gas hourly space velocity (GHSV) was fixed at 20,000 h<sup>-1</sup>. A multiple gas analyzer (Testo 350, Germany) was used for exhaust analysis to measure CO, NO, and NO<sub>2</sub> concentrations. The N<sub>2</sub>O concentrations were analyzed using a portable composite gas analyzer (PTM600, Shenzhen Eranntex Electronics Co., LTD). The NO conversion, CO conversion, and N<sub>2</sub> selectivity were evaluated as follows:

$$\eta_{\text{NO}_x}(\%) = \frac{[\text{NO}_x]_{\text{in}} - [\text{NO}_x]_{\text{out}}}{[\text{NO}_x]_{\text{in}}} \times 100\% \quad (1)$$

$$\eta_{\text{CO}}(\%) = \frac{[\text{CO}]_{\text{in}} - [\text{CO}]_{\text{out}}}{[\text{CO}]_{\text{in}}} \times 100\% \quad (2)$$

$$S_{\text{N}_2}(\%) = \left[ 1 - \frac{2[\text{N}_2\text{O}]_{\text{out}} + [\text{NO}_2]_{\text{out}}}{[\text{NO}_x]_{\text{in}} - [\text{NO}_x]_{\text{out}}} \right] \times 100\% \quad (3)$$

Where the “in” and “out” subscripts respectively represent the inlet and outlet concentrations of NO and CO in the steady-state.  $\eta_{\text{NO}_x}$  and  $\eta_{\text{CO}}$  are the NO<sub>x</sub> (NO and NO<sub>2</sub>) and CO conversion, respectively;  $S_{\text{N}_2}$  is the N<sub>2</sub> selectivity.

The reaction rate and activation energy ( $E_a$ ) over the catalysts were measured at a gas flow rate of 1 L min<sup>-1</sup> in the temperature range of 100–160 °C. To control  $\eta_{\text{NO}_x} < 15\%$ , the GHSVs used for Co<sub>3</sub>O<sub>4</sub>-CeO<sub>2</sub>, Co<sub>3</sub>O<sub>4</sub>-CeO<sub>2</sub>-IOV, and Co<sub>3</sub>O<sub>4</sub>-CeO<sub>2</sub>-IOV-C were 40,000 h<sup>-1</sup>, 60,000 h<sup>-1</sup>, and 55,000 h<sup>-1</sup>, respectively. The  $E_a$  was calculated using the Arrhenius equation. The specific reaction rate was evaluated by the following formula:

$$\text{Rate}(\text{mol}_{\text{NO}} \text{ g}_{\text{cat}}^{-1} \text{ h}^{-1}) = \frac{F \cdot (\text{L min}^{-1}) \times C_{\text{NO}}(\%) \times \eta_{\text{NO}}(\%)}{22.4(\text{L mol}^{-1}) \cdot m_{\text{cat}}(\text{g})} \times 60 \quad (4)$$

$F$  is the total volume flow rate;  $C_{\text{NO}}$  is the NO inlet volume fraction;  $m_{\text{cat}}$  is the mass of catalyst.

## 2.5. Computational detail

First-principles periodic DFT calculations were carried out using the CP2K code [24]. The core electrons are represented with norm-conserving Goedecker-Teter-Hutter pseudopotentials [25,26]. The valence electron wave function is expanded in a double-zeta basis set with polarization functions along with an auxiliary plane wave basis set with an energy cutoff of 400 Ry [27]. The generalized gradient approximation exchange-correlation function of Perdew, Burke, and

Enzerhof (PBE) is used [28]. The DFT-D3 scheme with an empirical damped potential term is added to the energies obtained from exchange-correlation functional in all calculations [29] to compensate for the long-range van der Waals (vdW) dispersion interaction. Transition states of elementary steps are located using the climbing image nudged elastic bands (CI-NEB) method. The computational details are listed in SI.

## 3. Results and discussion

### 3.1. Characterization of the catalysts

#### 3.1.1. XRD and PSD analysis

Fig. 1a shows the XRD patterns of all the catalysts. In the Co<sub>3</sub>O<sub>4</sub>-CeO<sub>2</sub> case, the observed main diffraction peaks at  $2\theta$  values of 28.6°, 33.1°, 47.5°, 56.3°, 59.1°, 69.4°, 76.7°, 79.1°, and 88.4° are indexed to the characteristic peaks of CeO<sub>2</sub> (JCPDS No. 034–0394), corresponding to the (111), (200), (220), (311), (222), (400), (331), (420), and (422) planes, respectively. The relatively weak diffraction peaks located at  $2\theta$  values of 19.0°, 31.4°, 36.9°, 38.6°, 44.9°, 59.5°, and 65.4° can be assigned to the (111), (220), (311), (222), (400), (511), and (440) planes of cubic-phased Co<sub>3</sub>O<sub>4</sub> (JCPDS No. 071–0816), respectively. Co<sub>3</sub>O<sub>4</sub>-CeO<sub>2</sub>-IOV and Co<sub>3</sub>O<sub>4</sub>-CeO<sub>2</sub>-IOV-C show identical diffraction patterns to Co<sub>3</sub>O<sub>4</sub>-CeO<sub>2</sub> but with a slight shift in the peak position of CeO<sub>2</sub> toward high values (Fig. 1b), implying the insertion of Co atoms with a smaller radius than Ce atoms into the lattice of CeO<sub>2</sub>. It is also noticed that the crystallinity of Co<sub>3</sub>O<sub>4</sub>-CeO<sub>2</sub>-IOV-C becomes higher than that of Co<sub>3</sub>O<sub>4</sub>-CeO<sub>2</sub>-IOV, implying that the atomic arrangement becomes ordered again after re-calcination. Fig. 1c displays the PSD curves of all the catalysts. The median diameters of Co<sub>3</sub>O<sub>4</sub>-CeO<sub>2</sub>, Co<sub>3</sub>O<sub>4</sub>-CeO<sub>2</sub>-IOV, and Co<sub>3</sub>O<sub>4</sub>-CeO<sub>2</sub>-IOV-C are 1.9 μm, 1.7 μm, and 1.7 μm, respectively. Meanwhile, all the catalysts had similar specific surface area and pore size distribution (Table 1). The above results indicate that the ball-milling process has no significant effect on particle size (Fig. S1), porous structure (Fig. S2 and Table 1), and crystallite size (Table 1).

#### 3.1.2. TEM observation

All the catalysts comprise primarily irregular spherical particles (Fig. 2a–c) with a sharp size distribution centered at 7–9 nm (Fig. S3). There are obvious interface regions in Co<sub>3</sub>O<sub>4</sub>-CeO<sub>2</sub> (Fig. 2a), Co<sub>3</sub>O<sub>4</sub>-CeO<sub>2</sub>-IOV (Fig. 2b), and Co<sub>3</sub>O<sub>4</sub>-CeO<sub>2</sub>-IOV-C (Fig. 2c). On both sides of the interface, the measured lattice distances of 0.24 nm and 0.29 nm can be well assigned to the Co<sub>3</sub>O<sub>4</sub> (311) and Co<sub>3</sub>O<sub>4</sub> (220) planes, respectively, and the lattice distances of 0.27 nm and 0.31 nm correspond to CeO<sub>2</sub> (200) and CeO<sub>2</sub> (111), indicating the formation of intimate contact interfaces between Co<sub>3</sub>O<sub>4</sub> and CeO<sub>2</sub> nanoparticles [19,30,31]. Upon a close observation by randomly enlarging one interface in Co<sub>3</sub>O<sub>4</sub>-CeO<sub>2</sub> (Fig. 2d), Co<sub>3</sub>O<sub>4</sub>-CeO<sub>2</sub>-IOV (Fig. 2e and Fig. S4), and Co<sub>3</sub>O<sub>4</sub>-CeO<sub>2</sub>-IOV-C (Fig. 2f), it is found that some atoms of the Co<sub>3</sub>O<sub>4</sub> phase and the CeO<sub>2</sub> phase are intertwined with each other. Furthermore, the arrangement of atoms at the interface becomes less ordered in Co<sub>3</sub>O<sub>4</sub>-CeO<sub>2</sub>-IOV and Co<sub>3</sub>O<sub>4</sub>-CeO<sub>2</sub>-IOV-C. The geometric phase analysis (GPA) further shows that the interface part of the Co<sub>3</sub>O<sub>4</sub>-CeO<sub>2</sub>-IOV nanoparticles is more compressible than the inner part, that is, the interface strain, which disturbs the Co and Ce arrays at the interface and induces lattice distortions (see the detailed description in SI). Moreover, compared to both Co<sub>3</sub>O<sub>4</sub>-CeO<sub>2</sub> (Fig. 2g) and Co<sub>3</sub>O<sub>4</sub>-CeO<sub>2</sub>-IOV-C (Fig. 2i), Co<sub>3</sub>O<sub>4</sub>-CeO<sub>2</sub>-IOV (Fig. 2h) shows a higher  $\epsilon_{xx}$  component of the strain tensor at the heterointerfaces, illustrating that there exists a greater interfacial strain in the latter. These results suggest that intimate interfacial contact between Co<sub>3</sub>O<sub>4</sub> and CeO<sub>2</sub> nanoparticles generates compressive strain [32,33], and the ball-milling process can facilitate this effect. The EDS mapping images obtained on large-scale TEM images of Co<sub>3</sub>O<sub>4</sub>-CeO<sub>2</sub> (Fig. 2j1–j4), Co<sub>3</sub>O<sub>4</sub>-CeO<sub>2</sub>-IOV (Fig. 2k1–k4), and Co<sub>3</sub>O<sub>4</sub>-CeO<sub>2</sub>-IOV-C (Fig. 2l1–l4) further evidence the generation of abundant interfaces between Co<sub>3</sub>O<sub>4</sub> and CeO<sub>2</sub> nanoparticles since there are obvious contact areas between

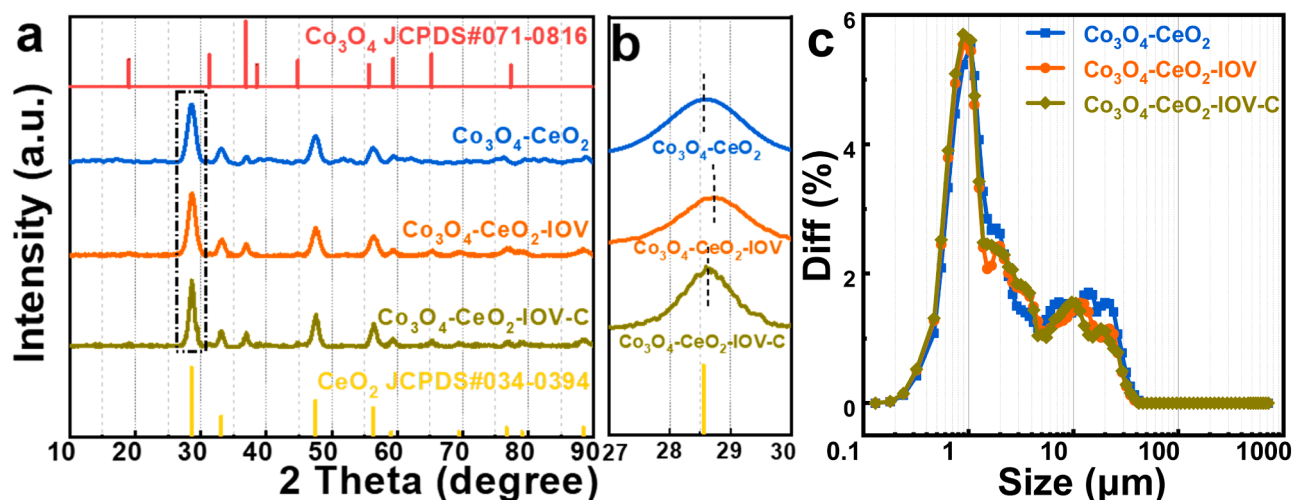


Fig. 1. XRD patterns (a), local enlargement of (a) in XRD (b), and PSD curves (c) of all the catalysts.

Table 1

Physical parameters of all the catalysts.

Sample	Crystallite size <sup>a</sup> (nm)	Lattice parameter <sup>a</sup> (Å)	Average grain size <sup>b</sup> (nm)	Particle size <sup>c</sup> (μm)	Surface area <sup>d</sup> (m <sup>2</sup> g <sup>-1</sup> )
Co <sub>3</sub> O <sub>4</sub> -CeO <sub>2</sub>	7.7	8.0654	7.8	1.9	33.3
Co <sub>3</sub> O <sub>4</sub> -CeO <sub>2</sub> -IOV	7.7	8.0627	7.9	1.7	32.3
Co <sub>3</sub> O <sub>4</sub> -CeO <sub>2</sub> -IOV-C	7.8	8.0624	8.0	1.7	39.0

<sup>a</sup> Estimated from the XRD diffraction peak ( $2\theta = 28.6^\circ$ ) for catalyst using the Debye-Scherrer equation.

<sup>b</sup> Average size calculated from more than 100 particles in TEM images.

<sup>c</sup> The particle size value of the catalysts from the laser particle analyser.

<sup>d</sup> Surface area derived from BET equation.

the Co and Ce elements. While for the distribution of O element, compared to both Co<sub>3</sub>O<sub>4</sub>-CeO<sub>2</sub> and Co<sub>3</sub>O<sub>4</sub>-CeO<sub>2</sub>-IOV-C, Co<sub>3</sub>O<sub>4</sub>-CeO<sub>2</sub>-IOV shows a much weaker O signal, consistent with its lower weight content of O in the EDS results (Fig. 2j<sub>6</sub>, k<sub>6</sub>, and l<sub>6</sub>), suggesting that some O atoms are lost. Therefore, the ball-milling process contributes to the generation of interfacial strain, which leads to the migration of O atoms, probably creating IOVs.

### 3.1.3. H<sub>2</sub>-TPR, O<sub>2</sub>-TPD, and EPR analysis

Fig. 3a presents the H<sub>2</sub>-TPR results of all the catalysts. The reduction peaks of all the catalysts are deconvoluted into four peaks as follows: peak T<sub>1</sub> (240–350 °C), attributed to the removal of surface adsorbed oxygen species; peak T<sub>2</sub> (350–400 °C), attributed to the reduction of Co<sup>3+</sup> at the interface between Co<sub>3</sub>O<sub>4</sub> and CeO<sub>2</sub> into Co<sup>2+</sup> [16,34]; peak T<sub>3</sub> (450–560 °C), attributed to the reduction of Co<sup>2+</sup> to Co in the structure of Co<sup>2+</sup>-OV-Co<sup>2+</sup> or Co<sup>2+</sup>-OV-Ce<sup>4+</sup> (OV represent oxygen vacancy) [16,34]; and peak T<sub>4</sub> (680–820 °C), attributed to the CeO<sub>2</sub> reduction to Ce<sup>3+</sup> [35]. Compared with those of Co<sub>3</sub>O<sub>4</sub>-CeO<sub>2</sub>, the reduction peaks of Co<sub>3</sub>O<sub>4</sub>-CeO<sub>2</sub>-IOV shift to higher temperatures after the ball-milling process, suggesting the generation of strong interaction between Co<sub>3</sub>O<sub>4</sub> and CeO<sub>2</sub> in this catalyst. In contrast, after the calcination, the reduction peaks of Co<sub>3</sub>O<sub>4</sub>-CeO<sub>2</sub>-IOV-C move to a lower temperature region than those of Co<sub>3</sub>O<sub>4</sub>-CeO<sub>2</sub>-IOV, implying that oxygen had filled the IOVs. Meanwhile, as shown in Table 2, the less H<sub>2</sub> consumption by the surface adsorbed oxygen species on Co<sub>3</sub>O<sub>4</sub>-CeO<sub>2</sub>-IOV than the other catalysts indicates an apparent oxygen migration

phenomenon through the ball-milling process. In addition, the third H<sub>2</sub> consumption peak in Co<sub>3</sub>O<sub>4</sub>-CeO<sub>2</sub>-IOV is the largest, implying the presence of the interactive interfaces (Co<sup>2+</sup>-OV-Ce<sup>4+</sup>) between Co<sub>3</sub>O<sub>4</sub> and CeO<sub>2</sub> [13], which cause the shift of the reduction of partial CeO<sub>2</sub> to the T<sub>3</sub> region. In short, the interaction between Co<sub>3</sub>O<sub>4</sub> and CeO<sub>2</sub> in Co<sub>3</sub>O<sub>4</sub>-CeO<sub>2</sub>-IOV was enhanced due to the presence of IOVs.

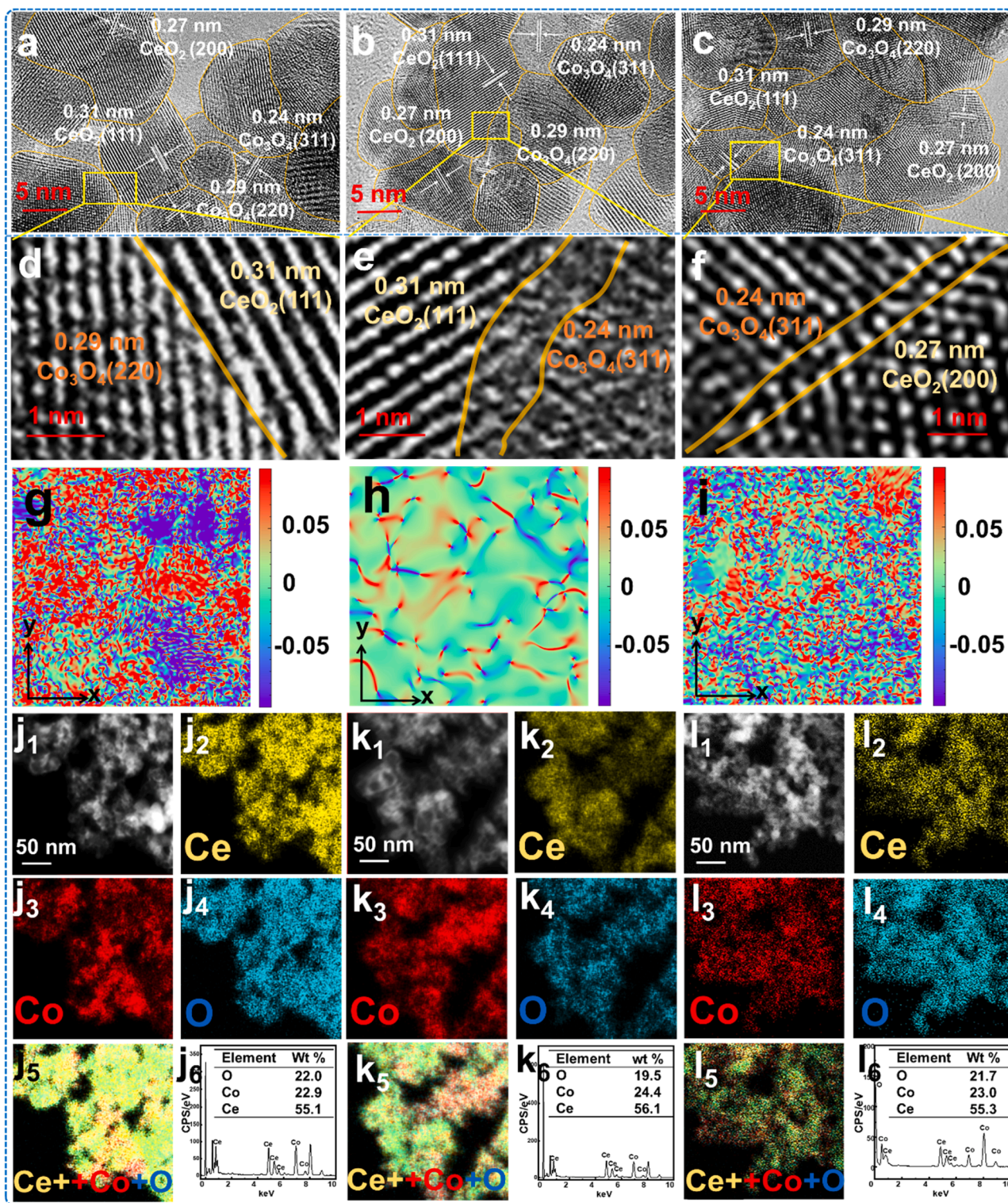
Fig. 3b shows the O<sub>2</sub>-TPD results of all the catalysts. Through the deconvolution of the curves, the desorption peaks of three catalysts are divided into three subpeaks (peak I, peak II, and peak III). The peak I is ascribed to the desorption of surface chemisorbed oxygen species (O<sup>2-</sup>, O<sub>2</sub><sup>-</sup>, and / or O<sup>-</sup>), peak II arises from surface lattice O (O<sub>2</sub><sup>-</sup>), and peak III belongs to the lattice O in bulk [31,34,36]. For these three catalysts, the content of surface chemisorbed oxygen species calculated by the peak area follows the order of Co<sub>3</sub>O<sub>4</sub>-CeO<sub>2</sub>-IOV (25.9%) > Co<sub>3</sub>O<sub>4</sub>-CeO<sub>2</sub>-IOV-C (16.2%) > Co<sub>3</sub>O<sub>4</sub>-CeO<sub>2</sub> (4.5%) (Table 2), and Co<sub>3</sub>O<sub>4</sub>-CeO<sub>2</sub>-IOV has the highest content of surface chemisorbed oxygen species, suggesting the presence of abundant OVs [18,30], probably related to the many generated grain boundaries between Co<sub>3</sub>O<sub>4</sub> and CeO<sub>2</sub> through the ball-milling. Compared with Co<sub>3</sub>O<sub>4</sub>-CeO<sub>2</sub> and Co<sub>3</sub>O<sub>4</sub>-CeO<sub>2</sub>-IOV-C, because of the presence of IOVs in Co<sub>3</sub>O<sub>4</sub>-CeO<sub>2</sub>-IOV, more oxygen was adsorbed by this sample during the oxygen pre-adsorption in the O<sub>2</sub>-TPD measurement, leading to a larger amount of oxygen desorption. In addition, the peak I and peak II of Co<sub>3</sub>O<sub>4</sub>-CeO<sub>2</sub>-IOV shift to lower temperatures, indicating that the OVs could be regenerated, which enhanced the oxygen migration capacity.

Fig. 3c shows the EPR spectra of all the catalysts. The two signals at  $g = 1.959$  and  $1.940$  in Co<sub>3</sub>O<sub>4</sub>-CeO<sub>2</sub> can be ascribed to Ce<sup>3+</sup>-O<sup>-</sup>-Ce<sup>4+</sup>-type defect sites located on the catalyst surface [37–39]. Co<sub>3</sub>O<sub>4</sub>-CeO<sub>2</sub>-IOV shows a new  $g$  value of 2.005, assigned to the signals of OVs in Co<sub>3</sub>O<sub>4</sub> [16], confirming some OVs in CeO<sub>2</sub> transferred to Co<sub>3</sub>O<sub>4</sub> after the ball milling. The coexistence of 1.959 and 2.005 implies the presence of OVs at the interface of the metal oxides. However, for Co<sub>3</sub>O<sub>4</sub>-CeO<sub>2</sub>-IOV-C, the signal at 1.959 disappears, and the one at 2.005 becomes very weak after calcination in the air because of the refilling of OVs by O<sub>2</sub> [40].

### 3.1.4. Raman and UV-vis analysis

Fig. 4a shows the Raman spectra of all the catalysts. The F<sub>2g</sub> band located at 462 cm<sup>-1</sup> can be attributed to the symmetric vibrating mode of the oxygen atoms around Ce ions in CeO<sub>2</sub>, and the D band at 600 cm<sup>-1</sup> is related to Ce<sup>3+</sup>-O<sup>-</sup>-Ce<sup>4+</sup>-type defect sites [41]. For Co<sub>3</sub>O<sub>4</sub>-CeO<sub>2</sub>-IOV, the intensity of the D band becomes higher than that of Co<sub>3</sub>O<sub>4</sub>-CeO<sub>2</sub>, indicating the replacement of Ce<sup>4+</sup> atoms by Ce<sup>3+</sup> atoms or impurity atoms in the bulk. On the other hand, the bands at 201 cm<sup>-1</sup>, 472 cm<sup>-1</sup>, 512 cm<sup>-1</sup>, and 687 cm<sup>-1</sup> correspond to the F<sub>1g</sub>, E<sub>g</sub>, F<sub>2g</sub>, and A<sub>1g</sub>





**Fig. 2.** TEM images of  $\text{Co}_3\text{O}_4$ - $\text{CeO}_2$  (a and d),  $\text{Co}_3\text{O}_4$ - $\text{CeO}_2$ -IOV (b and e), and  $\text{Co}_3\text{O}_4$ - $\text{CeO}_2$ -IOV-C (c and f);  $\epsilon_{xx}$  strain components of  $\text{Co}_3\text{O}_4$ - $\text{CeO}_2$  (g),  $\text{Co}_3\text{O}_4$ - $\text{CeO}_2$ -IOV (h), and  $\text{Co}_3\text{O}_4$ - $\text{CeO}_2$ -IOV-C (i) determined via geometric phase analysis; Ce, Co, and O elemental mappings and the EDS results recorded from individual  $\text{Co}_3\text{O}_4$ - $\text{CeO}_2$  (j1–j6),  $\text{Co}_3\text{O}_4$ - $\text{CeO}_2$ -IOV (k1–k6), and  $\text{Co}_3\text{O}_4$ - $\text{CeO}_2$ -IOV-C (l1–l6) particles.

symmetry modes of  $\text{Co}_3\text{O}_4$ , respectively [42,43]. The  $A_{1g}$  and  $F_{2g}^1$  bands can be assigned to the vibrations of  $\text{Co}^{3+}\text{-O}^{2-}$  and  $\text{Co}^{2+}\text{-O}^{2-}$ , respectively [42]. The  $E_g$  and  $F_{2g}^2$  bands are assigned to the  $\text{CoO}_6$  octahedral sites and  $\text{CoO}_4$  tetrahedral sites within the  $\text{Co}_3\text{O}_4$  lattice, respectively [14]. Compared with  $\text{Co}_3\text{O}_4$ - $\text{CeO}_2$  and  $\text{Co}_3\text{O}_4$ - $\text{CeO}_2$ -IOV-C,  $\text{Co}_3\text{O}_4$ - $\text{CeO}_2$ -IOV shows a red-shift of the  $E_g$  band ( $472\text{ cm}^{-1}$ ) and a lower

intensity of the  $A_{1g}$  band ( $687\text{ cm}^{-1}$ ) in Fig. 4b, which may be caused by a stronger interaction at the interface between  $\text{Co}_3\text{O}_4$  and  $\text{CeO}_2$  due to lattice distortion or interfacial strain [34]. Combining the above TEM and EPR characterization results, it can be confirmed that there exists interfacial strain in  $\text{Co}_3\text{O}_4$ - $\text{CeO}_2$ -IOV, which can provide the driving force for O migration, thereby forming IOVs.

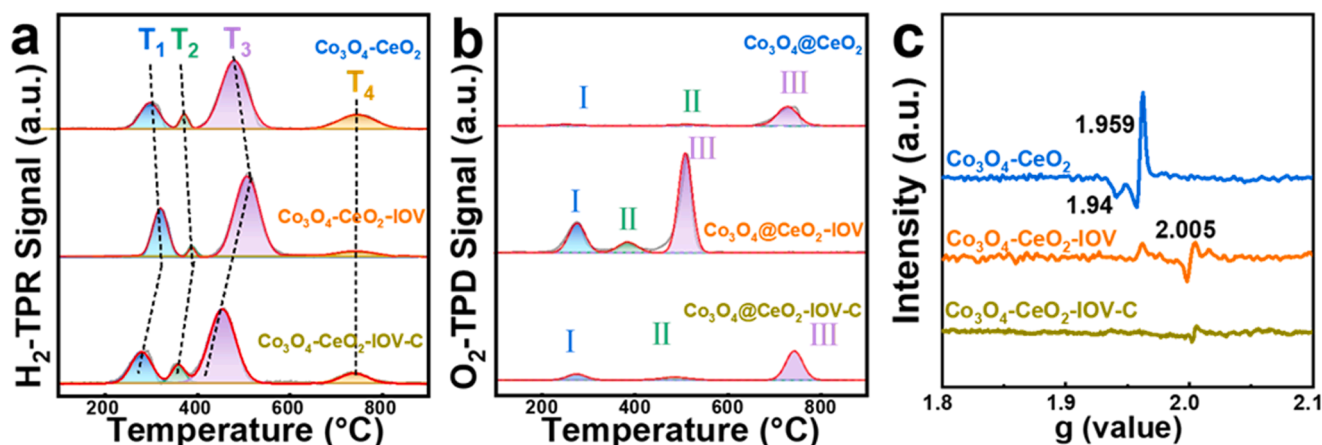


Fig. 3. H<sub>2</sub>-TPR (a), O<sub>2</sub>-TPD (b), and EPR (c) curves of all the catalysts.

Table 2

The amounts of H<sub>2</sub> consumption obtained by H<sub>2</sub>-TPR and O<sub>2</sub> desorption by O<sub>2</sub>-TPD for all the catalysts.

Sample	H <sub>2</sub> consumption (mmol g <sup>-1</sup> )				Total H <sub>2</sub> consumption (mmol g <sup>-1</sup> )	O <sub>2</sub> desorption (mmol g <sup>-1</sup> )			Total O <sub>2</sub> desorption (mmol g <sup>-1</sup> )
	T <sub>1</sub> peak	T <sub>2</sub> peak	T <sub>3</sub> peak	T <sub>4</sub> peak		I peak	II peak	III peak	
Co <sub>3</sub> O <sub>4</sub> -CeO <sub>2</sub>	0.73	0.27	2.66	0.71	4.37	0.01	0.01	0.15	0.17
Co <sub>3</sub> O <sub>4</sub> -CeO <sub>2</sub> -IOV	0.98	0.13	2.78	0.18	4.07	0.21	0.08	0.52	0.81
Co <sub>3</sub> O <sub>4</sub> -CeO <sub>2</sub> -IOV-C	0.85	0.35	2.62	0.49	4.31	0.03	0.02	0.14	0.19

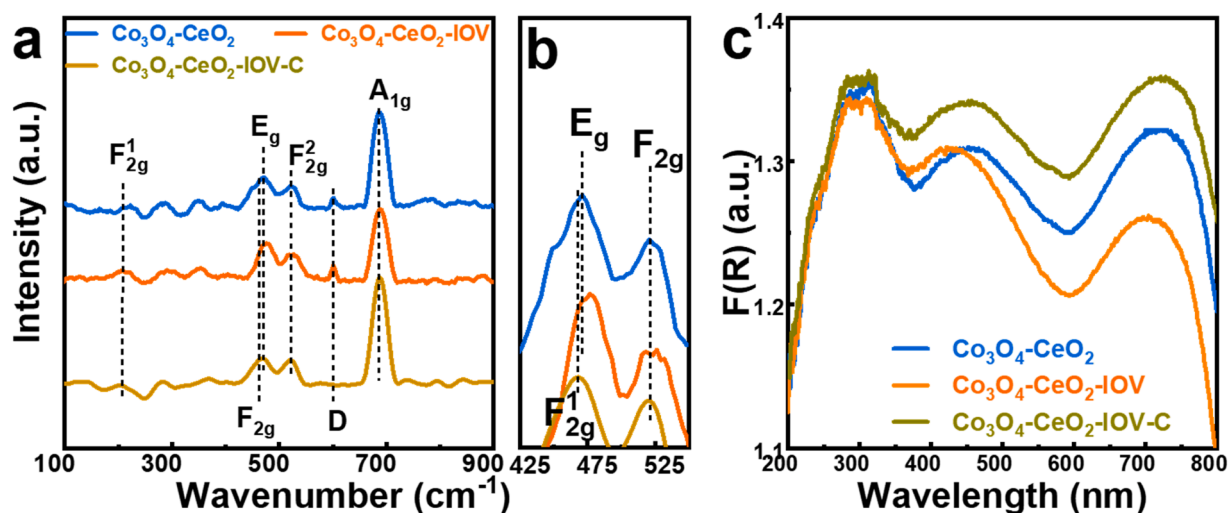


Fig. 4. Raman spectra (a), local enlargement of Raman (b), and UV-vis (c) of all the catalysts.

Fig. 4c shows the UV-vis diffuse reflection spectra of all the catalysts. Three absorption peaks are observed in the range of 200–350 nm, which are ascribed to  $\text{Ce}^{3+} \leftarrow \text{O}^{2-}$  charge transfer (255 nm),  $\text{Ce}^{4+} \leftarrow \text{O}^{2-}$  charge transfer (278 nm), and inter-band transitions (313 nm), respectively [41]. Moreover, the spectra also exhibit two broad bands at 400–550 and 650–800 nm, associated with the absorption of Co<sub>3</sub>O<sub>4</sub> [44]. It is noticed that the band at 400–550 nm, assigned to the  $^4\text{A}_2 \rightarrow ^4\text{T}_1$  (4 P) transition of Co<sup>2+</sup> species in tetrahedral coordination [16], exhibits a blue-shift for Co<sub>3</sub>O<sub>4</sub>-CeO<sub>2</sub>-IOV (430 nm) compared to that for Co<sub>3</sub>O<sub>4</sub>-CeO<sub>2</sub> (463 nm) and Co<sub>3</sub>O<sub>4</sub>-CeO<sub>2</sub>-IOV-C (460 nm). This is because of the stronger interfacial interactions between Co<sub>3</sub>O<sub>4</sub> and CeO<sub>2</sub> in the former, consistent with the H<sub>2</sub>-TPR and Raman results. As for the band at 650–800 nm related to the transitions from  $^4\text{A}_2(\text{F})$  to  $^4\text{T}_1(\text{G})$  of O<sup>2-</sup> species in tetrahedral coordination [16], it also has a blue-shift for Co<sub>3</sub>O<sub>4</sub>-CeO<sub>2</sub>-IOV (708 nm) compared to Co<sub>3</sub>O<sub>4</sub>-CeO<sub>2</sub> (726 nm) and

Co<sub>3</sub>O<sub>4</sub>-CeO<sub>2</sub>-IOV-C (728 nm), implying that Co<sub>3</sub>O<sub>4</sub>-CeO<sub>2</sub>-IOV possesses a lower oxygen migration barrier [16], further supporting the ball-milling process promotes the O migration.

### 3.1.5. XPS analysis

The XPS spectra of all the catalysts are presented in Fig. 5. The survey spectrum (Fig. 5a) indicates the presence of Co, Ce, and O, as well as C, which is used as the reference for binding energy calibration. As shown in Fig. 5b, the Co 2p spectra can be deconvoluted into six peaks with binding energy at 778.3 eV (2p<sub>3/2</sub>) and 793.4 eV (2p<sub>1/2</sub>), assigned to Co<sup>3+</sup> species, and 780.4 eV (2p<sub>3/2</sub>) and 795.9 eV plus two shake-up satellite peaks, assigned to Co<sup>2+</sup> species [30,34]. As summarized in Table 3, the Co<sup>2+</sup>/Co ratio decreases following the order of Co<sub>3</sub>O<sub>4</sub>-CeO<sub>2</sub>-IOV > Co<sub>3</sub>O<sub>4</sub>-CeO<sub>2</sub>-IOV-C > Co<sub>3</sub>O<sub>4</sub>-CeO<sub>2</sub>. On the other hand, the Ce 3d spectra in Fig. 5c exhibit two sets of 3d<sub>5/2</sub> and 3d<sub>3/2</sub> signals. The



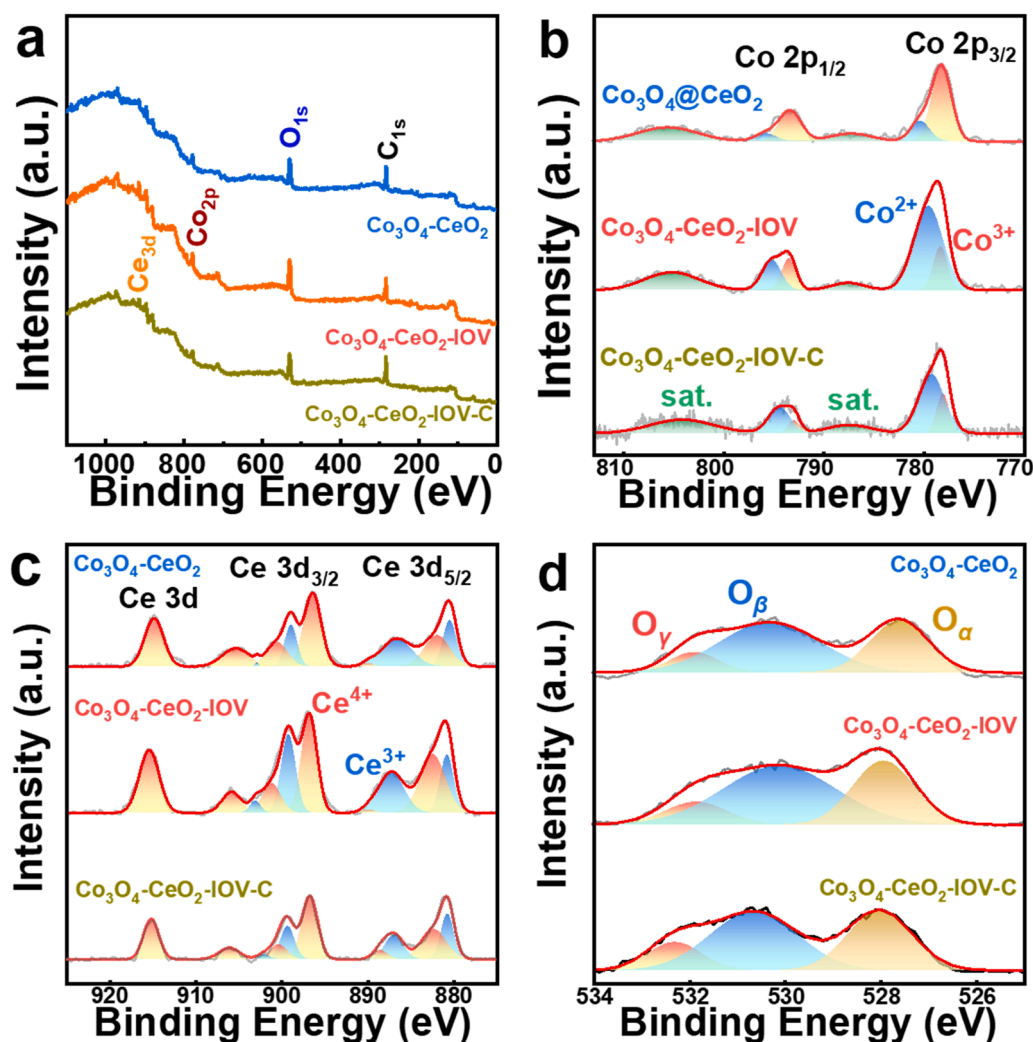


Fig. 5. Survey spectra (a), Co 2p (b), Ce 2p (c) and O 1s (d) XPS spectra of all the catalysts.

**Table 3**  
XPS results of all the catalysts.

Sample	Co <sup>2+</sup> / Co (%)	Ce <sup>3+</sup> / Ce (%)	O <sub>α</sub> / O (%)	O <sub>β</sub> / O (%)	Atomic composition (at%)		
					Co	Ce	O
Co <sub>3</sub> O <sub>4</sub> -CeO <sub>2</sub>	21.4	33.5	33.4	53.7	14.6	14.8	70.6
Co <sub>3</sub> O <sub>4</sub> -CeO <sub>2</sub> -IOV	79.9	37.4	32.7	55.5	19.7	19.4	60.9
Co <sub>3</sub> O <sub>4</sub> -CeO <sub>2</sub> -IOV-C	75.9	36.1	36.6	49.1	18.4	18.6	63.0

peaks at 882.2, 888.7, 896.6, 901.1, 906.0, and 915.2 eV are assigned to Ce<sup>4+</sup>, while the peaks at 880.7, 886.8, 899.2, and 902.6 eV belong to Ce<sup>3+</sup> [34]. The calculated contents of Ce<sup>3+</sup> and Ce<sup>4+</sup> by estimating the peak area are summarized in Table 3. As indicated, a higher concentration of surface Ce<sup>3+</sup> is also obtained on Co<sub>3</sub>O<sub>4</sub>-CeO<sub>2</sub>-IOV. In principle, the increase of Co<sup>2+</sup> species in Co<sub>3</sub>O<sub>4</sub>-CeO<sub>2</sub> composite oxides can be attributed to the following aspects: (1) the decrease of the number of O atoms connected to the Co species [13]; (2) the shift of the redox equilibrium ( $\text{Co}^{3+} + \text{Ce}^{3+} \leftrightarrow \text{Co}^{2+} + \text{Ce}^{4+}$ ) to the right due to the boosted electron transfer between Co<sup>3+</sup> and Ce<sup>3+</sup> [19]. Similarly, the increase of Ce<sup>3+</sup> can also be ascribed to (1) the decrease in the number of O atoms attached to the Ce species; (2) redox equilibrium ( $\text{Co}^{3+} + \text{Ce}^{3+} \leftrightarrow \text{Co}^{2+} + \text{Ce}^{4+}$ ) shifting to the left due to the enhanced electron transfer between Co<sup>2+</sup> and Ce<sup>4+</sup>. However, if both Co<sup>3+</sup> and Ce<sup>3+</sup> species are

increased simultaneously in one catalyst, there is only one explanation: the O atoms at the interface of Co and Ce are missing. Therefore, in the present study, the simultaneous increase of Co<sup>3+</sup> and Ce<sup>3+</sup> content in Co<sub>3</sub>O<sub>4</sub>-CeO<sub>2</sub>-IOV should be ascribed to the formation of abundant IOVs in this catalyst. Additionally, the fitted O 1s spectra in Fig. 5d display three different types of oxygen species: lattice O at 528.0 eV (O<sub>α</sub>), surface chemisorbed O species and OV at 530.6 eV (O<sub>β</sub>), and adsorbed water molecules at 532.3 eV (O<sub>γ</sub>). The lower surface O<sub>α</sub>/O ratio and higher surface O<sub>β</sub>/O ratio on Co<sub>3</sub>O<sub>4</sub>-CeO<sub>2</sub>-IOV than on Co<sub>3</sub>O<sub>4</sub>-CeO<sub>2</sub> and Co<sub>3</sub>O<sub>4</sub>-CeO<sub>2</sub>-IOV-C imply a lack of some surface lattice O atoms, but more abundant surface chemisorbed O species and OV in the former, in agreement with the above O<sub>2</sub>-TPD and H<sub>2</sub>-TPR results. Moreover, the corresponding XPS analysis (Table 3) indicates that the Co and Ce atomic weights in the three catalysts are close to the measured results by ICP-OES and the initial feeding ratio of the two precursors (Table S1).

### 3.1.6. XANES and EXAFS analysis

Fig. 6a shows the O K-edge X-ray absorption spectra of all the catalysts. The O K-edge XANES spectra can be fitted into three regions. The first region includes two peaks: peak A at approximately 532.5 eV and peak B at 534.5 eV. For all the catalysts, their peak shapes are very similar in this region. However, in the Co<sub>3</sub>O<sub>4</sub>-CeO<sub>2</sub>-IOV case, the intensity of peak A becomes weaker, and its position slightly shifts to lower energy compared to that of the other catalysts (insets in Fig. 6a). The second region is characterized by two scattering peaks of C

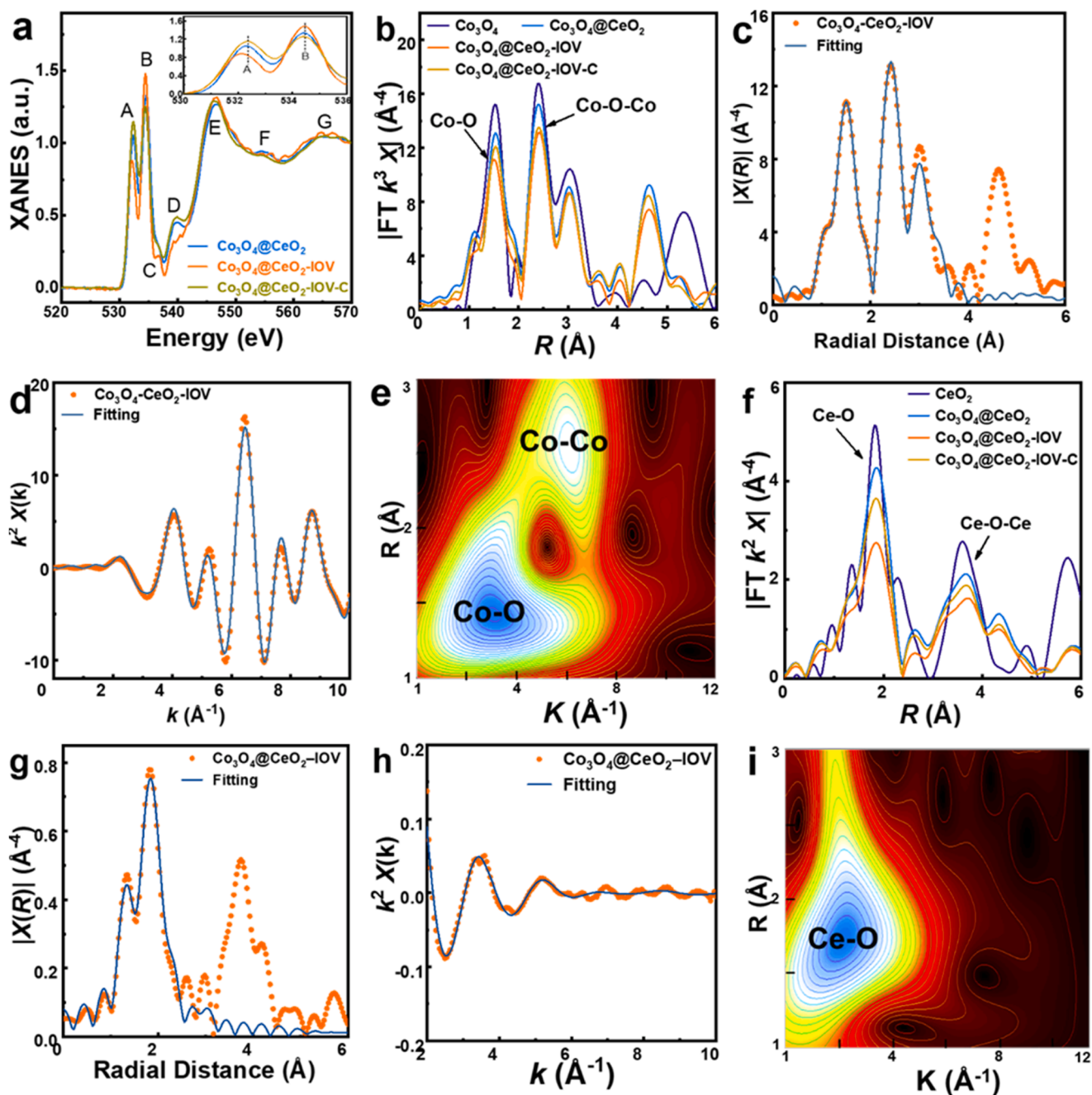


**Fig. 6.** Normalized O  $K$ -edge XANES spectra (a) and local enlargement of O  $K$ -edge XANES (insets in a); FT  $k^3$ -weighted of the Co  $K$ -edge EXAFS spectra (b), R space (c), and k space (d) EXAFS spectra, and WT-EXAFS contour plot of Co  $K$ -edge signals for the  $\text{Co}_3\text{O}_4$ -CeO<sub>2</sub>-IOV (e); FT  $k^2$ -weighted of the Ce  $L_{3}$ -edge EXAFS spectra (f), R space (g), k space (h), and WT-EXAFS contour plot of Ce  $L_{3}$ -edge signals for the  $\text{Co}_3\text{O}_4$ -CeO<sub>2</sub>-IOV (i).

(536.4 eV) and D (539.6 eV), with their intensity and width typically affected by both medium- and long-range order of catalysts [45]. In general, the presence of oxygen defects tends to broaden these two peaks due to the disorder in the local coordination [46]. Clearly, the peak D of  $\text{Co}_3\text{O}_4$ -CeO<sub>2</sub>-IOV is lower and wider than that of  $\text{Co}_3\text{O}_4$ -CeO<sub>2</sub> and  $\text{Co}_3\text{O}_4$ -CeO<sub>2</sub>-IOV-C, suggesting a decreased long-range order due to the formation of a large number of IOVs. The third region with an energy range of 550–570 eV contains three broad peaks of E, F, and G, respectively. These are basically the same in the three catalysts.

XAFS measurements were also used to investigate the coordination status of Co and Ce in the three catalysts. As shown in Fig. S5, for the Co  $K$ -edge XANES curves, the absorption edge of  $\text{Co}_3\text{O}_4$ -CeO<sub>2</sub>-IOV locates at the lowest energy among the three catalysts, implying a reduced valence

state of Co, consistent with the above Co 2p XPS results. Fig. 6b shows the Co  $K$ -edge EXAFS curves of all the catalysts using  $\text{Co}_3\text{O}_4$  as a reference. There are two prominent peaks at 1.53 Å and 2.39 Å, assigned to the coordination of Co-O and Co-Co, respectively. The intensities of the two peaks of  $\text{Co}_3\text{O}_4$ -CeO<sub>2</sub>-IOV are obviously lower than those in  $\text{Co}_3\text{O}_4$ -CeO<sub>2</sub> and  $\text{Co}_3\text{O}_4$ -CeO<sub>2</sub>-IOV-C, suggesting a decrease in the coordination number in  $\text{Co}_3\text{O}_4$ -CeO<sub>2</sub>-IOV [47]. Especially, the signal at ca. 1.53 Å for  $\text{Co}_3\text{O}_4$ -CeO<sub>2</sub>-IOV is observed with slight deformation compared with that of the other two catalysts, suggesting the formation of the Ce-Co interface [48]. The Quantitative EXAFS fitting is performed (Figs. 6c and 6d) and the structural parameters of Co in the  $\text{Co}_3\text{O}_4$ -CeO<sub>2</sub>-IOV are listed in Table S2. Moreover, a wavelet transform (WT) in Fig. 6e shows that  $\text{Co}_3\text{O}_4$ -CeO<sub>2</sub>-IOV displays two intensity maximums near  $\approx 3.0$  and



$6.0 \text{ \AA}^{-1}$  in  $k$  space attributed to the Co-O and Co-Co backscattering contributions.

In the Ce  $L_{3}$ -edge XANES curves of all the catalysts (Fig. S6),  $\text{Co}_3\text{O}_4$ - $\text{CeO}_2$ -IOV exhibits a lower intensity in absorption edge than  $\text{Co}_3\text{O}_4$ - $\text{CeO}_2$  and  $\text{Co}_3\text{O}_4$ - $\text{CeO}_2$ -IOV-C, suggesting a lower oxidation state of Ce in  $\text{Co}_3\text{O}_4$ - $\text{CeO}_2$ -IOV. Moreover, for all the catalysts, two main white-line absorption edges are observed around ca. 5730.9 and 5738.4 eV, attributed to a transition from Ce 2p $_{3/2}$  to the unoccupied Ce 5d state mixed with Ce 4f $^1$  and Ce 4f $^0$  final states [48], suggesting the coexistence of Ce $^{3+}$  and Ce $^{4+}$ . The continuum resonance is determined by a combination of Ce-Co scattering, which could arise from the independence of the Co doping [48]. The Ce  $L_{3}$ -edge EXAFS spectra of three catalysts are given in Fig. 6f, with pure  $\text{CeO}_2$  for comparison. The main sharp peaks at 1.67 Å and 3.44 Å are attributed to the scattering of Ce-O and Ce-O-Ce, respectively. Compared with the other two catalysts, the peak intensity of Ce-O coordination in  $\text{Co}_3\text{O}_4$ - $\text{CeO}_2$ -IOV is significantly decreased, indicating its higher concentration of OVs. Moreover, in the  $k^2$ -weighted EXAFS oscillations, the intensity of the Ce-Ce scattering peak is much weaker in  $\text{Co}_3\text{O}_4$ - $\text{CeO}_2$ -IOV than in the other two catalysts, verifying the attenuation of the second shell. This is because heterogeneous interfaces disturb the Ce and Co arrays and induce lattice distortions, thus suppressing the multiple scattering of photoelectrons [49, 50]. Quantitative EXAFS fitting is performed (Figs. 6g and 6h), and the structural parameters of Ce in the  $\text{Co}_3\text{O}_4$ - $\text{CeO}_2$ -IOV are listed in Table S2. Furthermore, the WT in Fig. 6i also shows that  $\text{Co}_3\text{O}_4$ - $\text{CeO}_2$ -IOV owns one intensity maximum near  $\approx 2.0 \text{ \AA}^{-1}$  in  $k$  space attributed to the Ce-O backscattering contribution. In short, the above results confirm the significant difference in the type and content of OVs in the three catalysts. There was a mutual exchange of  $\text{Co}_3\text{O}_4$  and  $\text{CeO}_2$  phases, which induced the formation of IOVs at the interface of  $\text{Co}_3\text{O}_4$  and  $\text{CeO}_2$  in  $\text{Co}_3\text{O}_4$ - $\text{CeO}_2$ -IOV, resulting in a change in the coordination environment.

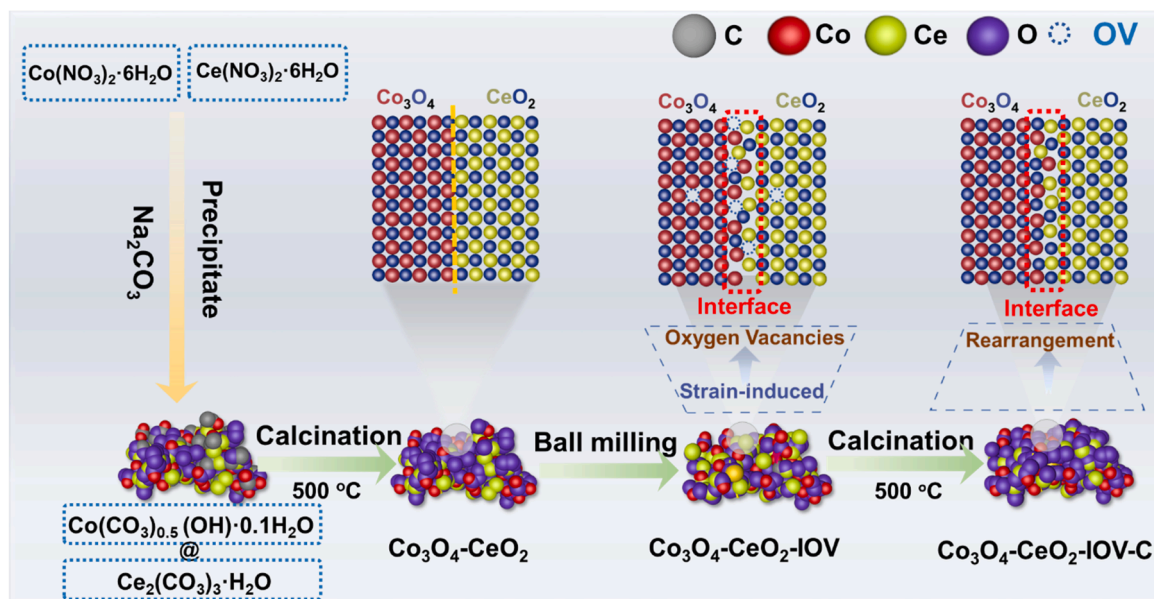
### 3.1.7. IOVs formation in the catalysts

According to the above structural characterizations, the formation of the IOVs-containing catalysts can be schematically illustrated in Scheme 1. Firstly, the  $\text{Co}(\text{NO}_3)_2$  and  $\text{Ce}(\text{NO}_3)_2$  precursors are mixed and react with  $\text{Na}_2\text{CO}_3$  to produce  $\text{Co}(\text{CO}_3)_{0.5}(\text{OH})_{0.1}\cdot\text{H}_2\text{O}$  and  $\text{Ce}(\text{CO}_3)_3\cdot\text{H}_2\text{O}$  precipitant mixture (Fig. S7a) by co-precipitation. After calcination in air at 500 °C (Fig. S7b), the precipitant mixture is decomposed into the  $\text{Co}_3\text{O}_4$ - $\text{CeO}_2$  catalyst with abundant heterointerfaces. Upon the

subsequent ball-milling process, strong mechanical strain and collision heat generated among nanoparticles lead to the particle shape distortion and the introduction of interfacial strain at the heterointerfaces, conducive to the formation of abundant IOVs in  $\text{Co}_3\text{O}_4$ - $\text{CeO}_2$ -IOV due to the weakening of the interfacial cation-oxygen bond strength [51]. Further calcining  $\text{Co}_3\text{O}_4$ - $\text{CeO}_2$ -IOV in air at 500 °C decreases IOVs in  $\text{Co}_3\text{O}_4$ - $\text{CeO}_2$ -IOV-C because of the filling of IOVs by oxygen. The corresponding results conform to the EPR analysis of the catalysts. It should be pointed out that, compared to the previously used strategies to create IOVs within the composite catalysts, including pulsed laser epitaxy [52], dopant segregation [53], hydrothermal route [54], and heat treatment [55], the ball-milling method is very simple and easily scalable, and being environment friendly (Table S3).

### 3.2. CO-SCR performances of the catalysts

Fig. 7 shows the catalytic performances of all the catalysts in CO-SCR in the presence of 5 vol%  $\text{O}_2$ . The  $\text{NO}_x$  conversion of all the catalysts exhibits a volcano-type tendency as the temperature increases (Fig. 7a). At each temperature (100–400 °C),  $\text{Co}_3\text{O}_4$ - $\text{CeO}_2$ -IOV delivers a higher NO conversion than  $\text{Co}_3\text{O}_4$ - $\text{CeO}_2$  and  $\text{Co}_3\text{O}_4$ - $\text{CeO}_2$ -IOV-C, particularly reaching 100%  $\text{NO}_x$  conversion in the temperature range of 200–350 °C. The CO conversion reaches 100% at above 150 °C for  $\text{Co}_3\text{O}_4$ - $\text{CeO}_2$ , but above 200 °C for  $\text{Co}_3\text{O}_4$ - $\text{CeO}_2$ -IOV-C, and above 250 °C for  $\text{Co}_3\text{O}_4$ - $\text{CeO}_2$ -IOV (Fig. 7b). Impressively, for  $\text{Co}_3\text{O}_4$ - $\text{CeO}_2$ -IOV, 100%  $\text{N}_2$  selectivity is obtained in the temperature range of 100–350 °C (Fig. 7c). Therefore,  $\text{Co}_3\text{O}_4$ - $\text{CeO}_2$ -IOV with the interfacial oxygen vacancies showed the best catalytic performance. In terms of the CO conversion, for the  $\text{Co}_3\text{O}_4$ - $\text{CeO}_2$  with only surface oxygen vacancies, in addition to the reduction reaction between NO and CO, a large amount of CO will be oxidized by  $\text{O}_2$  in this case. Therefore, it shows significantly lower NO conversion but higher CO conversion than the other two samples. The integral rate of  $\text{NO}_x$  conversion over  $\text{Co}_3\text{O}_4$ - $\text{CeO}_2$ -IOV is higher than that over  $\text{Co}_3\text{O}_4$ - $\text{CeO}_2$  and  $\text{Co}_3\text{O}_4$ - $\text{CeO}_2$ -IOV-C (Fig. 7d). As indicated in Fig. S8, in terms of the transient rate of  $\text{N}_2$  formation,  $\text{Co}_3\text{O}_4$ - $\text{CeO}_2$ -IOV still has obvious advantages compared with  $\text{Co}_3\text{O}_4$ -M and  $\text{CeO}_2$ -M. In contrast, for both  $\text{Co}_3\text{O}_4$ - $\text{CeO}_2$  and  $\text{Co}_3\text{O}_4$ - $\text{CeO}_2$ -IOV-C, their  $\text{N}_2$  selectivities quickly dropped after 150 °C. To confirm the role of IOVs in the reaction, we prepared the  $\text{Co}_3\text{O}_4$ + $\text{CeO}_2$  and  $\text{Co}_3\text{O}_4$ -M+ $\text{CeO}_2$ -M catalysts and measured their  $\text{NO}_x$  conversions (Fig. S9a), CO conversions (Fig. S9b), and  $\text{N}_2$  selectivities (Fig. S9c) under the same reaction conditions. Both



Scheme 1. Schematic illustration of the synthesis of all the catalysts.

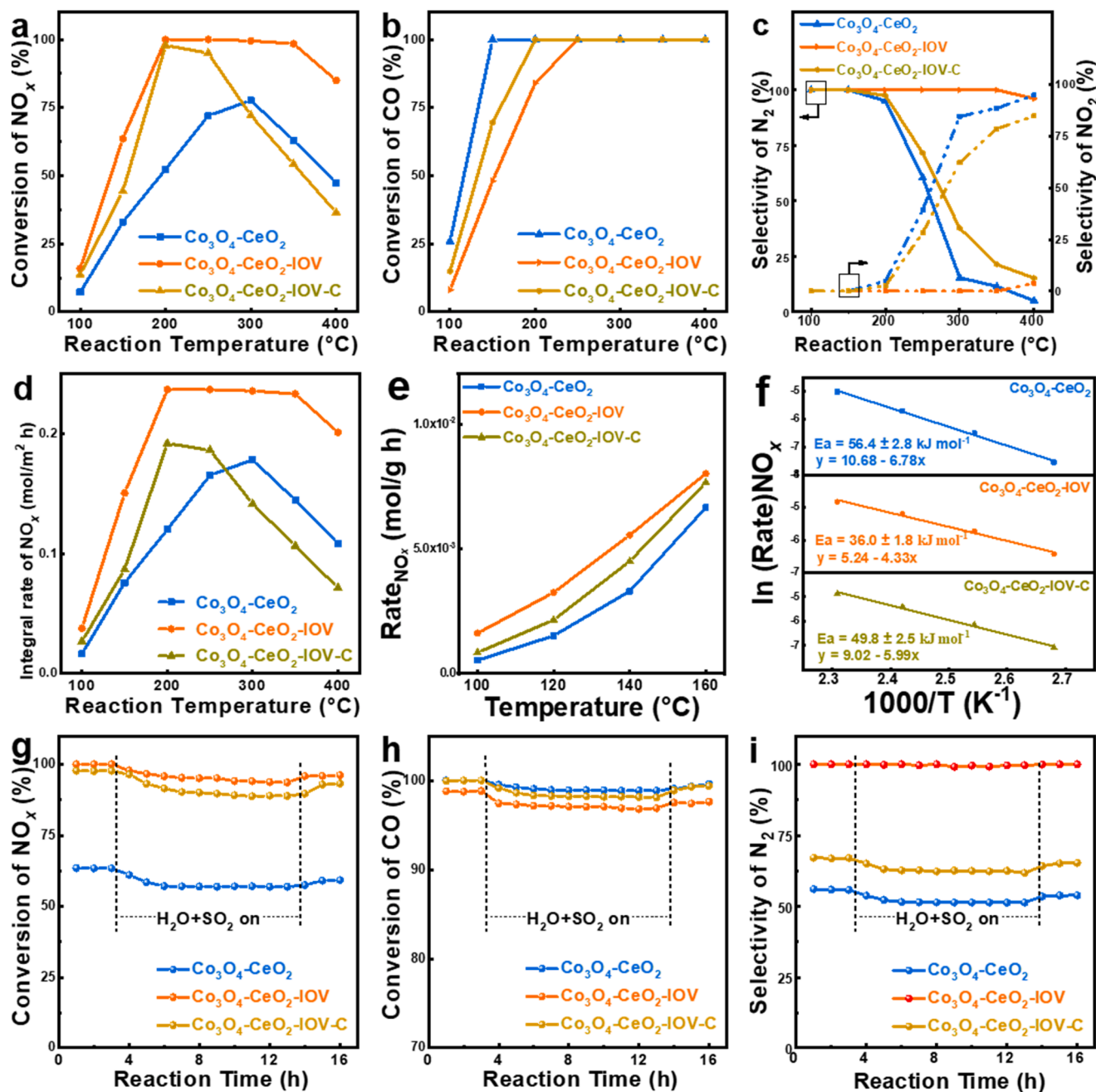


**Fig. 7.**  $\text{NO}_x$  conversion (a), CO conversion (b),  $\text{N}_2$  and  $\text{NO}_2$  selectivity (c), and integral rate of  $\text{NO}_x$  conversion (d) of all the catalysts as a function of reaction temperature in CO-SCR (reaction conditions:  $[\text{NO}] = 1000 \text{ ppm}$ ,  $[\text{CO}] = 2000 \text{ ppm}$ ,  $[\text{O}_2] = 5 \text{ vol\%}$ , and  $\text{N}_2$  as balanced gas, GHSV = 20,000  $\text{h}^{-1}$ ).  $\text{NO}_x$  consumption rate as a function of the reaction temperature (e), and Arrhenius plots for NO conversion (f) (reaction conditions:  $[\text{NO}] = 1000 \text{ ppm}$ ,  $[\text{CO}] = 2000 \text{ ppm}$ ,  $[\text{O}_2] = 5 \text{ vol\%}$ ,  $[\text{H}_2\text{O}(\text{g})] = 10 \text{ vol\%}$ , and  $\text{N}_2$  as balanced gas; the GHSVs of  $\text{Co}_3\text{O}_4\text{-CeO}_2$ ,  $\text{Co}_3\text{O}_4\text{-CeO}_2\text{-IOV}$ , and  $\text{Co}_3\text{O}_4\text{-CeO}_2\text{-IOV-C}$  are 40,000  $\text{h}^{-1}$ , 60,000  $\text{h}^{-1}$ , and 55,000  $\text{h}^{-1}$ , respectively). Long-term stability of  $\text{NO}_x$  conversion (g), CO conversion (h), and  $\text{N}_2$  selectivity (i) under  $\text{SO}_2$  and  $\text{H}_2\text{O}$  over the various catalysts (reaction conditions:  $[\text{NO}] = 1000 \text{ ppm}$ ,  $[\text{CO}] = 2000 \text{ ppm}$ ,  $[\text{O}_2] = 5 \text{ vol\%}$ ,  $[\text{H}_2\text{O}(\text{g})] = 10 \text{ vol\%}$ ,  $[\text{SO}_2] = 50 \text{ ppm}$ , and  $\text{N}_2$  as balanced gas,  $T = 250 \text{ }^\circ\text{C}$ , GHSV = 20,000  $\text{h}^{-1}$ ).

$\text{Co}_3\text{O}_4\text{-CeO}_2$  and  $\text{Co}_3\text{O}_4\text{-M+CeO}_2\text{-M}$  show much lower catalytic performance than  $\text{Co}_3\text{O}_4\text{-CeO}_2\text{-IOV}$ , confirming the significance of IOVs generated at the heterointerfaces of  $\text{Co}_3\text{O}_4$  and  $\text{CeO}_2$  in CO-SCR. It should be noted that, compared to the most reported catalysts,  $\text{Co}_3\text{O}_4\text{-CeO}_2\text{-IOV}$  shows superior catalytic performance in CO-SCR (see Table S4 and S5).

We further calculated the specific reaction rates and apparent activation energies to compare their intrinsic activities. Obviously,  $\text{Co}_3\text{O}_4\text{-CeO}_2\text{-IOV}$  has higher reaction rates than the other two catalysts at various temperatures (150–180  $^\circ\text{C}$ ) (Fig. 7e). Further experiments were conducted to confirm the absence of internal/external diffusion

limitations (Fig. S10). Additionally, the reactor internal diameter (8 mm) and the catalyst bed height (59.7 mm) were set to ensure that the catalytic reactions were properly measured in the kinetic regime. For instance, at 160  $^\circ\text{C}$ , the reaction rate over  $\text{Co}_3\text{O}_4\text{-CeO}_2\text{-IOV}$  is  $8.0 \times 10^{-3} \text{ mol}^{-1} \text{ g}_{\text{cat}}^{-1} \text{ h}^{-1}$ , much higher than that over  $\text{Co}_3\text{O}_4\text{-CeO}_2$  ( $6.7 \times 10^{-3} \text{ mol}^{-1} \text{ g}_{\text{cat}}^{-1} \text{ h}^{-1}$ ) and  $\text{Co}_3\text{O}_4\text{-CeO}_2\text{-IOV-C}$  ( $7.7 \times 10^{-3} \text{ mol}^{-1} \text{ g}_{\text{cat}}^{-1} \text{ h}^{-1}$ ). As shown in Fig. 7 f, the measured  $E_a$  values for  $\text{Co}_3\text{O}_4\text{-CeO}_2$ ,  $\text{Co}_3\text{O}_4\text{-CeO}_2\text{-IOV}$ , and  $\text{Co}_3\text{O}_4\text{-CeO}_2\text{-IOV-C}$  are  $56.4 \pm 2.8 \text{ kJ mol}^{-1}$ ,  $36.0 \pm 1.8 \text{ kJ mol}^{-1}$ , and  $49.8 \pm 2.5 \text{ kJ mol}^{-1}$ , respectively.  $\text{Co}_3\text{O}_4\text{-CeO}_2\text{-IOV}$  has the lowest  $E_a$  value, suggesting that this catalyst is more active than the other two catalysts. The kinetic reaction orders was measured over  $\text{Co}_3\text{O}_4\text{-CeO}_2$

IOV, following the empirical kinetic equation (Eq. S5). It shows that the reaction order of NO and CO over  $\text{Co}_3\text{O}_4\text{-CeO}_2\text{-IOV}$  is 0.03 and 0.98, respectively (Fig. S11), revealing that  $\alpha$  and  $\beta$  are close to zero order and first order, respectively, implying that gaseous CO mainly takes part and strong NO adsorption occurs over  $\text{Co}_3\text{O}_4\text{-CeO}_2\text{-IOV}$  in the CO-SCR reaction [56].

Fig. S12 shows the effect of  $\text{H}_2\text{O}$  (10 vol%) and  $\text{SO}_2$  (50 ppm) on the catalytic performance of all the catalysts in the presence of 5 vol%  $\text{O}_2$ . It can be seen that 10 vol%  $\text{H}_2\text{O}$  has no obvious effect on their  $\text{NO}_x$  conversions (Fig. S12a), CO conversions (Fig. S12b), and  $\text{N}_2$  selectivities (Fig. S12c), and  $\text{Co}_3\text{O}_4\text{-CeO}_2\text{-IOV}$  still shows much higher  $\text{NO}_x$  conversion and  $\text{N}_2$  selectivity than other two catalysts. Similarly, when 50 ppm  $\text{SO}_2$  is introduced into the reaction atmosphere,  $\text{Co}_3\text{O}_4\text{-CeO}_2\text{-IOV}$  still shows the best  $\text{SO}_2$ -tolerant performance regarding  $\text{NO}_x$  conversion (Fig. S12d) and  $\text{N}_2$  selectivity (Fig. S12f) with similar CO conversion levels (Fig. S12e). Furthermore, we investigated the effect of the coexistence of  $\text{H}_2\text{O}$  and  $\text{SO}_2$  in the feeding gas on the  $\text{NO}_x$  conversion (Fig. S12g), CO conversion (Fig. S12h), and  $\text{N}_2$  selectivity (Fig. S12i). All

the variation trends are similar to those observed for the single addition of  $\text{H}_2\text{O}$  (Figs. S12a-S12c) and  $\text{SO}_2$  (Figs. S12d-S12f).  $\text{NO}_x$  conversion on  $\text{Co}_3\text{O}_4\text{-CeO}_2\text{-IOV}$  (Fig. S12g) only decreases by less than 6.4% compared with the case without the addition of  $\text{H}_2\text{O}$  and  $\text{SO}_2$  (Fig. S12a) in the temperature range of 150 – 350 °C, and its  $\text{N}_2$  selectivity still remains 100% above 200 °C (Fig. S12i).

Moreover, we further examined the long-term resistance to  $\text{H}_2\text{O}$  and  $\text{SO}_2$  for all the catalysts at 250 °C. As shown in Fig. 7g,  $\text{Co}_3\text{O}_4\text{-CeO}_2\text{-IOV}$  initially shows approximately 100%  $\text{NO}_x$  conversion. After introducing 10 vol%  $\text{H}_2\text{O}$  and 50 ppm  $\text{SO}_2$ , the  $\text{NO}_x$  conversion on  $\text{Co}_3\text{O}_4\text{-CeO}_2\text{-IOV}$  remains approximately 94% in the period of 4–13 h but becomes a little lower on  $\text{Co}_3\text{O}_4\text{-CeO}_2$  (57%) and  $\text{Co}_3\text{O}_4\text{-CeO}_2\text{-IOV-C}$  (89%). When  $\text{H}_2\text{O}$  and  $\text{SO}_2$  are switched off, the  $\text{NO}_x$  conversion on  $\text{Co}_3\text{O}_4\text{-CeO}_2$ ,  $\text{Co}_3\text{O}_4\text{-CeO}_2\text{-IOV}$ , and  $\text{Co}_3\text{O}_4\text{-CeO}_2\text{-IOV-C}$  recover to 59%, 96%, and 93%, respectively. The CO conversion exhibits a similar tendency on  $\text{Co}_3\text{O}_4\text{-CeO}_2\text{-IOV}$  and  $\text{Co}_3\text{O}_4\text{-CeO}_2\text{-IOV-C}$ , except for a smaller degradation (Fig. 7h). The  $\text{N}_2$  selectivity decreases from the initial 100% to 99.2% for  $\text{Co}_3\text{O}_4\text{-CeO}_2\text{-IOV}$ , from 56.1% to 51.3% for  $\text{Co}_3\text{O}_4\text{-CeO}_2\text{-IOV-C}$ , and

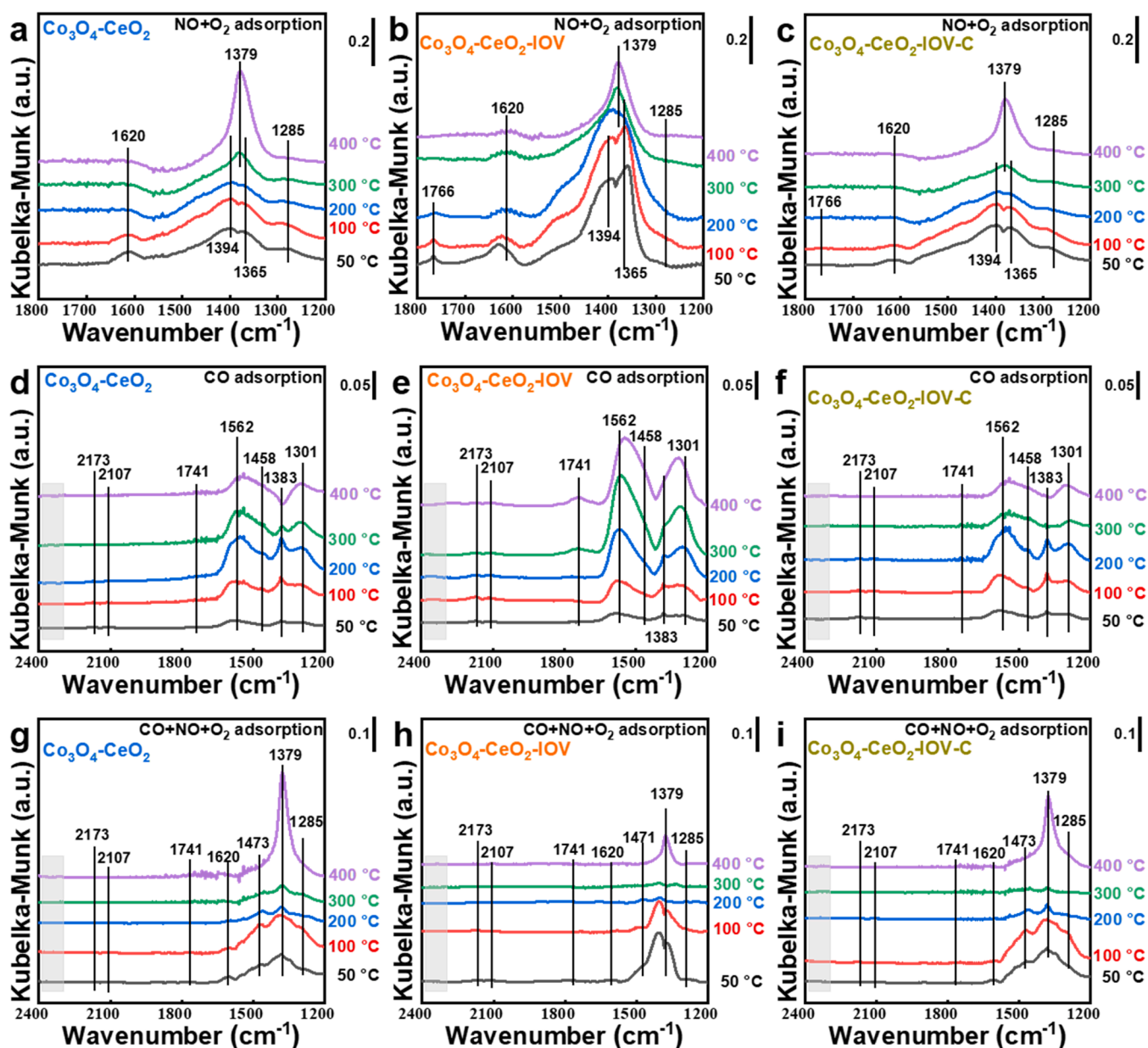


Fig. 8. *In situ* DRIFTS spectra showing adsorption of 1000 ppm NO + 5 vol%  $\text{O}_2$  or / and 2000 ppm CO onto various catalysts.



from 67.0% to 62.4% for Co<sub>3</sub>O<sub>4</sub>-CeO<sub>2</sub>-IOV-C (Fig. 7i). Additionally, the XRD pattern (Fig. S13a) and TEM images (Figs. S13b and S13c) of Co<sub>3</sub>O<sub>4</sub>-CeO<sub>2</sub>-IOV indicate no obvious change in the structure even after the activity tests at 250 °C for 16 h in an environment containing 5 vol % O<sub>2</sub>, 10 vol% H<sub>2</sub>O, and 50 ppm SO<sub>2</sub>, confirming its excellent stability. This catalyst was further tested according to industrial standards at different O<sub>2</sub> concentrations (1, 5, or 10 vol%), as shown in Fig. S14, which also retains excellent catalytic properties. In addition, the catalyst was also treated in the hydrothermal aging condition (denoted as Co<sub>3</sub>O<sub>4</sub>-CeO<sub>2</sub>-IOV-aged) at 250 °C and compared with Co<sub>3</sub>O<sub>4</sub>-CeO<sub>2</sub>-IOV for CO-SCR, as shown in Fig. S15. It can be seen that the two catalysts show quite similar and excellent catalytic performances.

### 3.3. In situ DRIFTS measurement

*In situ* DRIFTS experiments of NO + O<sub>2</sub> adsorption were performed at various temperatures (50–400 °C) to investigate the interaction of NO with the catalysts. In the cases of NO + O<sub>2</sub> adsorption on Co<sub>3</sub>O<sub>4</sub>-CeO<sub>2</sub> (Fig. 8a), Co<sub>3</sub>O<sub>4</sub>-CeO<sub>2</sub>-IOV (Fig. 8b), and Co<sub>3</sub>O<sub>4</sub>-CeO<sub>2</sub>-IOV-C (Fig. 8c) at 50 °C, intensive bands at 1365 and 1394 cm<sup>-1</sup> are observed, which are ascribed to the formation of nitrite and nitrate, respectively [57]. With increasing temperature, these peaks shift to 1379 cm<sup>-1</sup>, characteristic of the free nitrate ion [58], which may be due to the transformation of unstable nitro species to more thermally stable nitrates species. In all the cases, the peak intensities of nitrite and nitrate species continuously increase with the temperature until 300 °C. Furthermore, compared with that on Co<sub>3</sub>O<sub>4</sub>-CeO<sub>2</sub> and Co<sub>3</sub>O<sub>4</sub>-CeO<sub>2</sub>-IOV-C, the peak intensities of NO species at 1365, 1379, and 1394 cm<sup>-1</sup> on Co<sub>3</sub>O<sub>4</sub>-CeO<sub>2</sub>-IOV are much stronger, while the adsorption peak of the chelating bidentate nitrite at 1285 cm<sup>-1</sup> is weaker. The peaks at 1620 cm<sup>-1</sup> belong to NO<sub>2</sub>, and the one at 1766 cm<sup>-1</sup> to N<sub>2</sub>O<sub>4</sub>. It is worth mentioning that the oxidation of NO to NO<sub>x</sub> species (NO<sub>2</sub> and N<sub>2</sub>O<sub>4</sub> species) is relevant to surface adsorbed oxygen (O<sup>-</sup> or O<sub>2</sub><sup>-</sup>, O<sub>2</sub>). The larger the amount of the oxygen species adsorbed on the surface, the more NO<sub>x</sub> species are produced on the surface.

The *in situ* DRIFTS spectra of CO adsorption on the catalyst surface with increasing temperature from 50 to 400 °C were measured. For Co<sub>3</sub>O<sub>4</sub>-CeO<sub>2</sub> (Fig. 8d), Co<sub>3</sub>O<sub>4</sub>-CeO<sub>2</sub>-IOV (Fig. 8e), and Co<sub>3</sub>O<sub>4</sub>-CeO<sub>2</sub>-IOV-C (Fig. 8f), the bands at 1301 and 1741 cm<sup>-1</sup> are attributed to mono-carbonates and carbonyl vibration [57], respectively. It is worth noting that Co<sub>3</sub>O<sub>4</sub>-CeO<sub>2</sub>-IOV exhibits a stronger carbonyl vibration peak. The bands at 1383, 1458, and 1562 cm<sup>-1</sup> are ascribed to the vibrations of the adsorbed carboxylate ( $\nu_s(\text{COO}^-)$ ,  $\nu_{as}(\text{CO}_3^{2-})$ , and  $\nu_{as}(\text{COO}^-)$  [58], respectively, and their intensities keep stable and are independent of the temperature because of their high stability. For Co<sub>3</sub>O<sub>4</sub>-CeO<sub>2</sub>-IOV, the peaks with the maximum intensities are observed at 1301 and 1562 cm<sup>-1</sup>. Two peaks at 2173 and 2107 cm<sup>-1</sup> are observed for the tested catalysts, and these two peaks are assigned to the P and R branches of gaseous CO [59]. The bands observed at 2320–2380 cm<sup>-1</sup> are the characteristic vibrations of physically adsorbed or gaseous CO<sub>2</sub> [59], implying that the CO reacted with surface-active oxygen species on the catalyst surface to generate CO<sub>2</sub>. Moreover, as the reaction temperature increases, the intensity of these peaks becomes lower, attributed to the desorption of physically adsorbed CO<sub>2</sub>. Also, it shows that the IOVs are beneficial to the reaction of CO and the activation of oxidation species (i.e., NO<sub>x</sub> or O<sub>2</sub>).

The *in situ* DRIFTS spectra of co-adsorbed CO and NO + O<sub>2</sub> on Co<sub>3</sub>O<sub>4</sub>-CeO<sub>2</sub> (Fig. 8g), Co<sub>3</sub>O<sub>4</sub>-CeO<sub>2</sub>-IOV (Fig. 8h), and Co<sub>3</sub>O<sub>4</sub>-CeO<sub>2</sub>-IOV-C (Fig. 8i) were measured under simulated reaction conditions. Both CO and NO + O<sub>2</sub> are observed with similar peak positions to those in the individual adsorption. Comparing the adsorption of NO + O<sub>2</sub> (Figs. 8a–8c) with the case of NO + O<sub>2</sub> and CO (Figs. 8g–8i) on all the catalysts, the carbonates species (1309, 1458, 1541, and 1741 cm<sup>-1</sup>) are observed but decreased in intensity in the latter case, and in particular, the peak at 1458 cm<sup>-1</sup> is disappeared, indicating that the formed carbonates decreased in intensity or even disappeared when NO existed in the flue

gas. The IR bands that decreased in intensity correspond to active adsorbed NO<sub>x</sub> intermediates formed during the NO + CO + O<sub>2</sub> reaction that eventually led to N<sub>2</sub>, N<sub>2</sub>O, and NO<sub>2</sub>, whereas those that did not decrease correspond to inactive (spectator) adsorbed NO<sub>x</sub> species. This proves that the reaction between CO and adsorbed NO<sub>x</sub> also occurs on the surface of the catalyst (Fig. S16) [60–62]. Comparing Co<sub>3</sub>O<sub>4</sub>-CeO<sub>2</sub> with Co<sub>3</sub>O<sub>4</sub>-CeO<sub>2</sub>-IOV-C (Fig. S17), it is found that the peak of N<sub>2</sub>O (2426 cm<sup>-1</sup>) on Co<sub>3</sub>O<sub>4</sub>-CeO<sub>2</sub>-IOV almost disappeared at 200–300 °C, but reappeared at 400 °C, consistent with the results of N<sub>2</sub> selectivity in CO-SCR performance. Moreover, comparing Figs. 8d–8f with Figs. 8g–8i, the peaks at 2173 and 2107 cm<sup>-1</sup>, corresponding to gaseous CO, decrease significantly, indicating the occurrence of the reaction between CO and the intermediate. Combined with the results of the pre-adsorption experiment (Fig. S18) show that the negative IR bands (1571 cm<sup>-1</sup>) appear after NO + O<sub>2</sub> adsorption in Fig. S18b, which is due to NO adsorption on the Co<sup>2+</sup> site of Ce-IOV-Co, resulting in the decrease of Co<sup>2+</sup> on the surface of the Co<sub>3</sub>O<sub>4</sub>-CeO<sub>2</sub>-IOV catalyst. With the introduction of CO, NO\* dissociates and reacts with CO, and the negative IR bands recover. Therefore, IOVs in the catalyst play a key role in adsorbing NO and weakening the N-O bond.

### 3.4. DFT calculations

DFT calculations were performed to investigate the formation energy of OV on Co<sub>3</sub>O<sub>4</sub>-CeO<sub>2</sub>-IOV. As shown in Table S6, creating a surface oxygen site is generally more facile than creating an OV in the bulk metal oxide. The formation energy difference between the surface and the subsurface OVs for the CeO<sub>2</sub> (111), Co<sub>3</sub>O<sub>4</sub> (111) and CeCoO<sub>4</sub> (111) surfaces is 71.2 kJ/mol, 90.8 kJ/mol, and 121.8 kJ/mol, respectively. This energy difference in OV formation can be regarded as the driving force for the OV migration from the subsurface to the surface. The larger the energy difference, the more likely the migration of OVs from the subsurface to the surface will be. As such, it is expected that more OVs would be formed on the Co<sub>3</sub>O<sub>4</sub>-CeO<sub>2</sub>-IOV catalyst.

In the present work, NO reduction by CO is carried out under O<sub>2</sub>-containing conditions. The OVs are not only the active site for NO decomposition but also for oxygen activation. As shown in Fig. S19, the adsorbed oxygen molecule is activated via the O-O bond breaking, forming the oxygen adatom bonding at the Ce/Co metal site, while the other oxygen atom fills the vacancy site. The calculated activation barriers for oxygen activation are 63.7 kJ/mol, 44.7 kJ/mol, and 51.6 kJ/mol over CeO<sub>2</sub>(111)\_OV, Co<sub>3</sub>O<sub>4</sub>(111)\_OV, and CeCoO<sub>4</sub>(111)\_IOV, respectively (the optimized structures of the model in Fig. S20). Compared with oxygen activation, NO decomposition is kinetically more favorable on Co<sub>3</sub>O<sub>4</sub>(111)\_OV and CeCoO<sub>4</sub>(111)\_IOV with lower energy barriers (37.6 and 38.0 kJ/mol). At the same time, oxygen adsorption and activation are thermodynamically and kinetically favorable over NO decomposition on the CeO<sub>2</sub>(111)\_OV. This suggests that oxygen activation would eliminate the OVs site, which is active for NO decomposition. Therefore, oxygen activation may inhibit NO reduction by CO over the CeO<sub>2</sub>(111)\_OV under the O<sub>2</sub>-containing conditions.

To reveal the role of OVs in the NO reduction over Co<sub>3</sub>O<sub>4</sub> and CeO<sub>2</sub> composite oxides, we compared the reduction of NO by CO over the perfect CeCoO<sub>4</sub>(111) and the defective CeCoO<sub>4</sub>(111)\_IOV. Fig. 9a shows the electronic localization function (ELF) contour maps of CeCoO<sub>4</sub>(111) and CeCoO<sub>4</sub>(111)\_IOV. The higher ELF value observed at the OV site indicates the highly localized charge density after creating OVs. The OVs can be a potential electron donor for the neighboring site, which is beneficial to the reduction of NO. To obtain further insight into how the OVs affect the NO reduction, the NO reduction by CO over CeCoO<sub>4</sub>(111) and CeCoO<sub>4</sub>(111)\_IOV are investigated, as shown in Fig. 9b. The structures of all intermediates and transition states are given in Figs. S21 and S22. Firstly, the calculated NO adsorption energies on CeCoO<sub>4</sub>(111) and CeCoO<sub>4</sub>(111)\_IOV are -99.1 kJ/mol and -179.5 kJ/mol, respectively, suggesting that the presence of OVs dramatically boost the NO



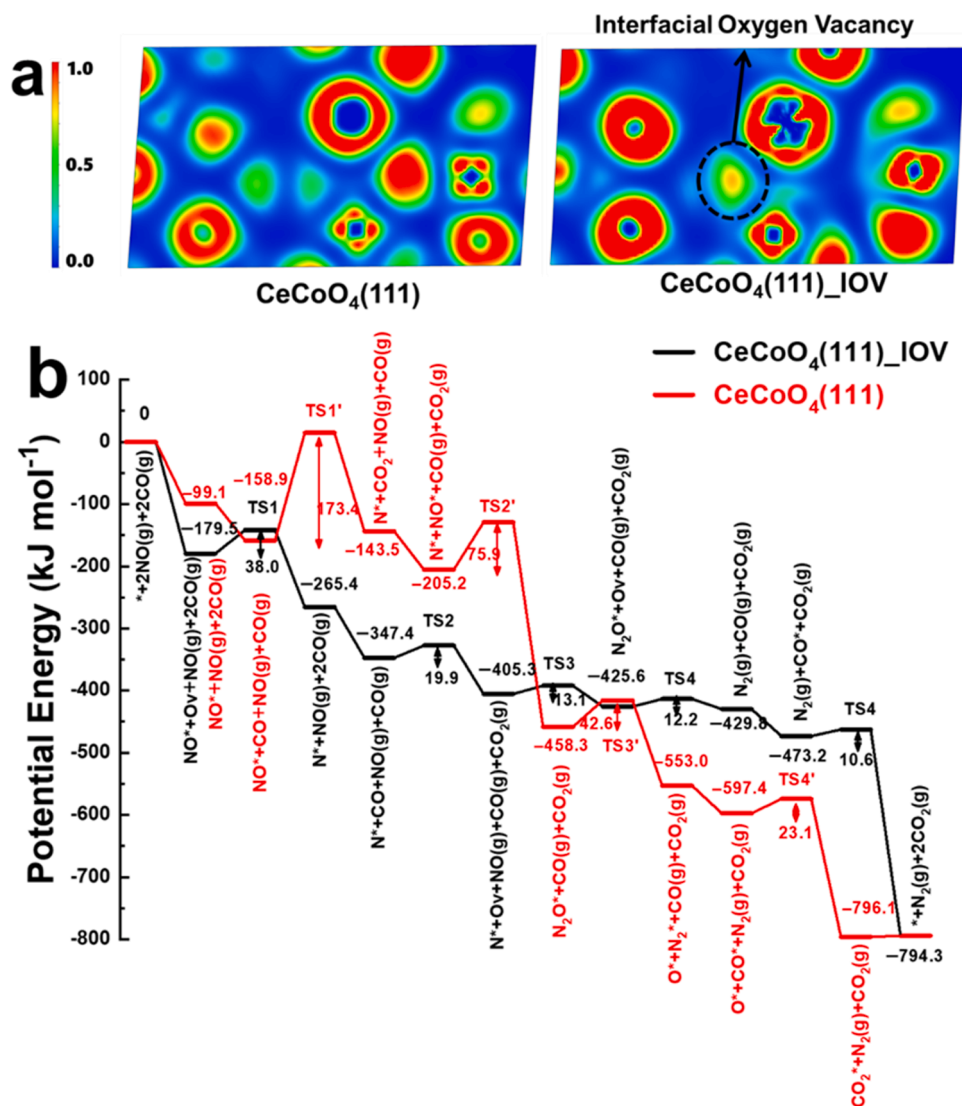


**Fig. 9.** Effect of the oxygen vacancy on the catalytic NO reduction by CO in the presence of O<sub>2</sub>. The ELF contours of the CeCoO<sub>4</sub>(111) and CeCoO<sub>4</sub>(111)\_IOV catalysts (a); DFT calculated reaction energy profiles for 2NO(g) + 2CO(g) → N<sub>2</sub>(g) + 2CO<sub>2</sub>(g) over CeCoO<sub>4</sub>(111) and CeCoO<sub>4</sub>(111)\_IOV (b).

adsorption. Then, the strongly adsorbed NO\* decomposes into atomic N\* and O\* with an activation barrier of 38.0 kJ/mol over CeCoO<sub>4</sub>(111)\_IOV. The atomic O\* interacts with a coming CO molecule to form the first CO<sub>2</sub> molecule (corresponding results of kinetic measurement). The decomposition of the adsorbed NO\* into N\* and O\* is the rate-limiting step in the NO reduction over the CeO<sub>2</sub>(111)\_OV (Fig. S23), Co<sub>3</sub>O<sub>4</sub>(111)\_OV (Fig. S24), and CeCoO<sub>4</sub>(111)\_IOV (Fig. 9b). The calculated reaction barrier for the formation of the first CO<sub>2</sub> molecule is 19.9 kJ/mol, indicating that the NO activation and CO<sub>2</sub> formation are kinetically facile over the CeCoO<sub>4</sub>(111)\_IOV. While on the CeCoO<sub>4</sub>(111), the formation of the first CO<sub>2</sub> molecule is kinetically unfavorable, with a very high activation energy of 173.4 kJ/mol. Next, a NO molecule is introduced to the CeCoO<sub>4</sub>(111)\_IOV system to interact with the adatom N\* to form an N<sub>2</sub>O\* intermediate, a phenomenon confirmed by *in situ* DRIFTS experimental observation. This step is kinetically more favorable with a lower activation barrier of 12.2 kJ/mol than that over CeCoO<sub>4</sub>(111) (75.9 kJ/mol). Subsequently, the formed N<sub>2</sub>O\* intermediate decomposes into an N<sub>2</sub> molecule and an adatom O\*. DFT calculations show that the N<sub>2</sub> formation over CeCoO<sub>4</sub>(111)\_IOV is more feasible with an activation barrier of 12.2 kJ/mol, lower than that over CeCoO<sub>4</sub>(111) (42.6 kJ/mol). The generation of the second CO<sub>2</sub> molecule over both CeCoO<sub>4</sub>(111) and CeCoO<sub>4</sub>(111)\_IOV is facile with

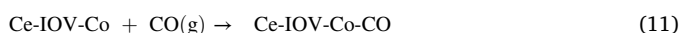
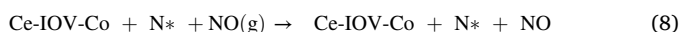
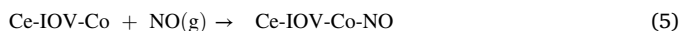
small activation barriers of 10.6 kJ/mol and 23.1 kJ/mol and large energy releases of -321.1 kJ/mol and -198.7 kJ/mol, respectively. As shown in Fig. 9b, the complete reduction of NO by CO is highly exothermic, with a reaction change of -794.3 kJ/mol.

In order to examine the influence of OVs on the NO and CO oxidation, we investigated the NO and CO oxidation via O<sub>2</sub> over CeCoO<sub>4</sub>(111)\_IOV using DFT calculations. As shown in Fig. S25, the calculated co-adsorption energies for NO/CO and O<sub>2</sub> co-adsorbed on the surface of CeCoO<sub>4</sub>(111)\_IOV are -185.9 and -123.9 kJ/mol, respectively, and the activation barriers for the formation of NO<sub>2</sub> and CO<sub>2</sub> are 102.0 and 113.7 kJ/mol. Compared with the CO-SCR pathway with the highest reaction barrier of 38 kJ/mol for NO\* decomposition (Fig. 9b), NO and CO oxidation via O<sub>2</sub> are kinetically unfavorable due to the very high activation barriers. These results clearly indicate that the CO-SCR reaction pathway over CeCoO<sub>4</sub>(111)\_IOV catalyst is more prone to occur, rather than NO and CO oxidation via O<sub>2</sub>.

### 3.5. Proposed mechanism for the CO-SCR reaction

Based on the above analysis, the CO-SCR process can be described by nine elementary reaction steps. Here, gaseous species (g), adsorbed species (\*), the interface of Co<sub>3</sub>O<sub>4</sub> and CeO<sub>2</sub> containing OVs (Co-IOV-

Ce), and the interface of  $\text{Co}_3\text{O}_4$  and  $\text{CeO}_2$  without IOVs (Co-O-Ce) are represented. NO is first adsorbed on the IOVs of the catalyst (Eq. 1), then the N-O bond is dissociated to form  $\text{Co-O-Ce} + \text{N}^*$  (Eq. 2). Based on kinetic measurements and *in situ* DRIFTS results, gaseous CO is directly involved in the reaction. The reaction of gaseous CO with  $\text{Co-O-Ce} + \text{N}^*$  results in the formation of  $\text{Co-IOV-Ce} + \text{N}^*$  and gaseous  $\text{CO}_2$  (Eq. 3). After that, the second NO molecule adsorbs on  $\text{Co-IOV-Ce} + \text{N}^*$  (Eq. 4), which reacts with  $\text{N}^*$  to  $\text{N}_2\text{O}$  (Eq. 5). The formation of  $\text{N}_2\text{O}$  requires the adsorption and dissociation of NO (i.e. Eqs. 1–5 of the elementary reaction), which needs the joint action of the  $\text{Co}_3\text{O}_4\text{-CeO}_2\text{-IOV}$  catalyst and heat. This is why the  $\text{N}_2\text{O}$  formation can be observed at 100 °C. The elementary reaction expressed in Eq. 6 is  $\text{N}_2\text{O}$  decomposition on IOV, which also requires energy input by heating. Our experiments prove that the effective working temperature range for IOV is 200–350 °C, which is the reason for the disappearance of  $\text{N}_2\text{O}$  at 200–300 °C. As the temperature increases to 400 °C, the  $\text{N}_2\text{O}$  peak appears again, which may be because that  $\text{O}_2$  is activated and reacts with CO to form  $\text{CO}_2$  (based on the CO conversion in Fig. 7b), resulting in a weaker CO reduction  $\text{Ce-O-Co}$  reaction and the lack of IOV decomposition of  $\text{N}_2\text{O}$ . Finally, the second CO molecule adsorbs on the Co site of  $\text{Co-IOV-Ce}$  and then reacts with  $\text{O}^*$  to generate the second  $\text{CO}_2$  molecule, and regenerates IOVs for completing the entire the  $2\text{NO}(\text{g}) + 2\text{CO}(\text{g}) = 2\text{CO}_2(\text{g}) + \text{N}_2(\text{g})$  redox reaction cycle (Eqs. 7 and 8).



Compared with  $\text{Co}_3\text{O}_4\text{-CeO}_2$  composite oxides without IOVs, the IOVs in the  $\text{Co}_3\text{O}_4\text{-CeO}_2\text{-IOV}$  can promote NO adsorption with larger adsorption energy. The  $\text{O}_2$  adsorption energy on the  $\text{Co}_3\text{O}_4\text{-CeO}_2\text{-IOV}$  catalyst is smaller than that of the NO adsorption; thus, the NO molecule would preferably occupy the IOVs to avoid  $\text{O}_2$  activation. This explains why the  $\text{Co}_3\text{O}_4\text{-CeO}_2\text{-IOV}$  catalyst has excellent  $\text{N}_2$  selectivity under  $\text{O}_2$ -containing conditions. Moreover, IOVs have a strong recovery ability because  $\text{Co-O-Ce}$  easily reacts with CO to form  $\text{Co-IOV-Ce}$ . The results show that the NO activation and IOVs formation are kinetically facile over the  $\text{Co}_3\text{O}_4\text{-CeO}_2\text{-IOV}$  catalyst.

#### 4. Conclusions

The  $\text{Co}_3\text{O}_4\text{-CeO}_2\text{-IOV}$  catalyst with abundant IOVs is successfully developed by inducing interfacial strain through ball-milling. It shows approximately 94%  $\text{NO}_x$  conversion and 100%  $\text{N}_2$  selectivity in the temperature range of 200–350 °C (5 vol%  $\text{O}_2$ , 10 vol%  $\text{H}_2\text{O}$ , 50 ppm  $\text{SO}_2$ , and 20,000  $\text{h}^{-1}$ ), much better than  $\text{Co}_3\text{O}_4\text{-CeO}_2$  and  $\text{Co}_3\text{O}_4\text{-CeO}_2\text{-IOV-C}$ . The investigation of the adsorption behaviors of different gases by *in situ* DRIFTS indicates that IOVs in the catalyst play a key role in NO dissociation. The DFT calculation reveals that IOVs within  $\text{Co}_3\text{O}_4\text{-CeO}_2\text{-IOV}$  are more favorable for the rate-limiting step, NO adsorption and dissociation, especially compared with  $\text{O}_2$  activation. This work demonstrates the importance of the strategic design of IOVs within composite oxide catalysts to boost the CO-SCR reaction, especially under  $\text{O}_2$ -containing conditions.

#### CRediT authorship contribution statement

**Shaomian Liu:** Methodology, Validation, Formal analysis, Investigation, Data curation, Writing – original draft, Visualization. **Wenjuan Xue:** Calculations. **Yongjun Ji:** Conceptualization, Writing – review & editing, Visualization, Supervision, Project administration, Funding acquisition. **Wenqing Xu:** Resources, Funding acquisition. **Wenxing Chen:** XAS analysis. **Lihua Jia:** Data curation. **Tingyu Zhu:** Resources, Funding acquisition. **Ziyi Zhong:** Writing – review & editing. **Guangwen Xu:** Resources. **Donghai Mei:** Calculations, Resources. **Fabing Su:** Conceptualization, Methodology, Writing – review & editing, Visualization, Supervision, Project administration, Funding acquisition.

#### Declaration of Competing Interest

The authors declare that they have no known competing financial interests or personal relationships that could have appeared to influence the work reported in this paper.

#### Data availability

Data will be made available on request.

#### Acknowledgements

We gratefully acknowledge the financial supports from the National Natural Science Foundation of China (Nos. 52070180, 51938014, 52222005, and 91961119), the Science Research Project of the Ministry of Education of the Heilongjiang Province of China (No. 145109102), and the Beijing Chenxi Environmental Engineering Co. Ltd., Z. Z. thanks the financial support of Guangdong Key discipline fund in 2022 for this collaboration. Y. J. thanks the financial supports from the Outstanding Youth cultivation program of Beijing Technology and Business University (No. 19008021144) and Research Foundation for Advanced Talents of Beijing Technology and Business University (No. 19008020159).

#### Appendix A. Supporting information

Supplementary data associated with this article can be found in the online version at doi:10.1016/j.apcatb.2022.122151.

#### References

- [1] Y. Inomata, H. Kubota, S. Hata, E. Kiyonaga, T. Murayama, Bulk tungsten-substituted vanadium oxide for low-temperature  $\text{NO}_x$  removal in the presence of water, *Nat. Commun.* 12 (2021) 557.
- [2] T. Andana, K.G. Rappé, F. Gao, J. Szanyi, X. Pereira-Hernandez, Y. Wang, Recent advances in hybrid metal oxide-zeolite catalysts for low-temperature selective catalytic reduction of  $\text{NO}_x$  by ammonia, *Appl. Catal. B-Environ.* 291 (2021), 120054.
- [3] I. Heo, Y.W. You, J.H. Lee, S.J. Schmiege, D.Y. Yoon, C.H. Kim, Urealess  $\text{NO}_x$  reduction by carbon monoxide in simulated lean-burn exhausts, *Environ. Sci. Technol.* 54 (2020) 8344–8351.
- [4] Z. Gholami, G. Luo, F. Gholami, F. Yang, Recent advances in selective catalytic reduction of  $\text{NO}_x$  by carbon monoxide for flue gas cleaning process: a review, *Catal. Rev.* 63 (2020) 68–119.
- [5] L. Han, S. Cai, M. Gao, J.Y. Hasegawa, P. Wang, J. Zhang, L. Shi, D. Zhang, Selective catalytic reduction of  $\text{NO}_x$  with  $\text{NH}_3$  by using novel catalysts: state of the art and future prospects, *Chem. Rev.* 119 (2019) 10916–10976.
- [6] L. Dong, L. Zhang, C. Sun, W. Yu, J. Zhu, L. Liu, B. Liu, Y. Hu, F. Gao, L. Dong, Y. Chen, Study of the properties of  $\text{CuO}/\text{VO}_x/\text{TiO}_2\text{SnO}_5\text{O}_2$  catalysts and their activities in NO + CO reaction, *ACS Catal.* 1 (2011) 468–480.
- [7] K.L. Pan, C.W. Young, G.T. Pan, M.B. Chang, Catalytic reduction of NO by CO with Cu-based and Mn-based catalysts, *Catal. Today* 348 (2020) 15–25.
- [8] S. Zhang, J. Shan, Y. Zhu, L. Nguyen, W. Huang, H. Yoshida, S. Takeda, F.F. Tao, Restructuring transition metal oxide nanorods for 100% selectivity in reduction of nitric oxide with carbon monoxide, *Nano Lett.* 13 (2013) 3310–3314.
- [9] C. Tang, B. Sun, J. Sun, X. Hong, Y. Deng, F. Gao, L. Dong, Solid state preparation of  $\text{NiO-CeO}_2$  catalyst for NO reduction, *Catal. Today* 281 (2017) 575–582.
- [10] C.A. Sierra-Pereira, E.A. Urquiza-González, Reduction of NO with CO on CuO or  $\text{Fe}_2\text{O}_3$  catalysts supported on  $\text{TiO}_2$  in the presence of  $\text{O}_2$ ,  $\text{SO}_2$  and water steam, *Fuel* 118 (2014) 137–147.

- [11] X. Dai, W. Jiang, W. Wang, X. Weng, Y. Shang, Y. Xue, Z. Wu, Supercritical water syntheses of transition metal-doped CeO<sub>2</sub> nano-catalysts for selective catalytic reduction of NO by CO: An in situ diffuse reflectance Fourier transform infrared spectroscopy study, *Chinese, J. Catal.* 39 (2018) 728–735.
- [12] H. Inomata, M. Shimokawabe, A. Kuwana, M. Arai, Selective reduction of NO with CO in the presence of O<sub>2</sub> with Ir/WO<sub>3</sub> catalysts: Influence of preparation variables on the catalytic performance, *Appl. Catal. B-Environ.* 84 (2008) 783–789.
- [13] X. Wang, S. Zhao, Y. Zhang, Z. Wang, J. Feng, S. Song, H. Zhang, CeO<sub>2</sub> nanowires self-inserted into porous Co<sub>3</sub>O<sub>4</sub> frameworks as high-performance “noble metal free” hetero-catalysts, *Chem. Sci.* 7 (2016) 1109–1114.
- [14] J. Zeng, X. Zhong, J. Yu, T. Zhang, Y. Wang, H. Chang, Promotional effect of preparation methods on catalytic reduction of NO by CO over CoCeO<sub>x</sub> catalysts, *Ind. Eng. Chem. Res.* 59 (2019) 34–41.
- [15] S. Liu, Y. Ji, W. Xu, J. Zhang, R. Jiang, L. Li, L. Jia, Z. Zhong, G. Xu, T. Zhu, F. Su, Hierarchically interconnected porous Mn<sub>3</sub>Co<sub>3-x</sub>O<sub>4</sub> spinels for Low-temperature catalytic reduction of NO by CO, *J. Catal.* 406 (2022) 72–86.
- [16] X. Wang, X. Li, J. Mu, S. Fan, X. Chen, L. Wang, Z. Yin, M. Tade, S. Liu, Oxygen vacancy-rich porous Co<sub>3</sub>O<sub>4</sub> nanosheets toward boosted NO reduction by CO and CO oxidation: Insights into the structure-activity relationship and performance enhancement mechanism, *ACS Appl. Mater. Inter.* 11 (2019) 41988–41999.
- [17] S. Li, X. Chen, F. Wang, Z. Xie, Z. Hao, L. Liu, B. Shen, Promotion effect of Ni doping on the oxygen resistance property of Fe/CeO<sub>2</sub> catalyst for CO-SCR reaction: Activity test and mechanism investigation, *J. Hazard. Mater.* 431 (2022), 128622.
- [18] Z. Su, W. Si, H. Liu, S. Xiong, X. Chu, W. Yang, Y. Peng, J. Chen, X. Cao, J. Li, Boosting the catalytic performance of CeO<sub>2</sub> in toluene combustion via the Ce-Ce homogeneous interface, *Environ. Sci. Technol.* 55 (2021) 12630–12639.
- [19] B. Qiu, C. Wang, N. Zhang, L. Cai, Y. Xiong, Y. Chai, CeO<sub>2</sub>-induced interfacial Co<sup>2+</sup> octahedral sites and oxygen vacancies for water oxidation, *ACS Catal.* 9 (2019) 6484–6490.
- [20] Z. Zhang, I. Karimata, H. Nagashima, S. Muto, K. Ohara, K. Sugimoto, T. Tachikawa, Interfacial oxygen vacancies yielding long-lived holes in hematite mesocrystal-based photoanodes, *Nat. Commun.* 10 (2019) 4832.
- [21] P. Jing, P. Liu, M. Hu, X. Xu, B. Liu, J. Zhang, Formation of interfacial Cu-[O<sub>2</sub>]-Ce structures with oxygen vacancies for enhanced electrocatalytic nitrogen reduction, *Small* (2022), e2201200.
- [22] J. He, P. Wu, Y. Wu, H. Li, W. Jiang, S. Xun, M. Zhang, W. Zhu, H. Li, Taming interfacial oxygen vacancies of amphiphilic tungsten oxide for enhanced catalysis in oxidative desulfurization, *ACS Sustain. Chem. Eng.* 5 (2017) 8930–8938.
- [23] C. Shen, Q. Bao, W. Xue, K. Sun, Z. Zhang, X. Jia, D. Mei, C. Liu, Synergistic effect of the metal-support interaction and interfacial oxygen vacancy for CO<sub>2</sub> hydrogenation to methanol over Ni/In<sub>2</sub>O<sub>3</sub> catalyst: A theoretical study, *J. Energy Chem.* 65 (2022) 623–629.
- [24] T.D. Kuhne, M. Iannuzzi, M. Del Ben, V.V. Rybkin, P. Seewald, F. Stein, T. Laino, R. Z. Khalullin, O. Schutt, F. Schiffmann, D. Golze, J. Wilhelm, S. Chulkov, M. H. Bani-Hashemian, V. Weber, U. Borstnik, M. Taillefumier, A.S. Jakobovits, A. Lazzaro, H. Pabst, T. Muller, R. Schade, M. Guidon, S. Andermatt, N. Holmberg, G.K. Schenter, A. Hehn, A. Bussy, F. Belleflamme, G. Tabacchi, A. Gloss, M. Lass, I. Bethune, C.J. Mundy, C. Plessl, M. Watkins, J. VandeVondele, M. Krack, J. Hutter, CP2K: An electronic structure and molecular dynamics software package - Quickstep: efficient and accurate electronic structure calculations, *J. Chem. Phys.* 152 (2020), 194103.
- [25] S. Goe De Cker, M. Teter, J. Hutter, Separable dual-space Gaussian pseudopotentials, *Phys. Rev. B Condens. Matter* 54 (1995) 1703–1710.
- [26] C. Hartwigsen, S. Goedecker, J. Hutter, Relativistic separable dual-space Gaussian Pseudopotentials from H to Rn, *Phys. Rev. B* 58 (1998) 3641–3662.
- [27] J. VandeVondele, J. Hutter, Gaussian basis sets for accurate calculations on molecular systems in gas and condensed phases, *J. Chem. Phys.* 127 (2007) 4365–4477.
- [28] J.P. Perdew, K. Burke, M. Ernzerhof, Generalized gradient approximation made simple, *Phys. Rev. Lett.* 77 (1998) 3865–3868.
- [29] S. Grimme, J. Antony, S. Ehrlich, H. Krieg, A consistent and accurate ab initio parametrization of density functional dispersion correction (DFT-D) for the 94 elements H-Pu, *J. Chem. Phys.* 132 (2010), 154104.
- [30] X. Feng, F. Luo, Y. Chen, D. Lin, Y. Luo, L. Xiao, X. Liu, X. Sun, Q. Qian, Q. Chen, Boosting total oxidation of propane over CeO<sub>2</sub>@Co<sub>3</sub>O<sub>4</sub> nanofiber catalysts prepared by multifluidic coaxial electrospraying with continuous grain boundary and fast lattice oxygen mobility, *J. Hazard. Mater.* 406 (2021), 124695.
- [31] L. Zhu, S. Pan, Z. Liu, P. Wei, Z. Liu, P. Yu, Y. Xu, Effect of rare earth metal (RE = La, Pr, Nd, Y) doping on Co-Ce composite oxide and its application in catalytic combustion of chlorobenzene, *Ind. Eng. Chem. Res.* 59 (2020) 5686–5698.
- [32] J. Mao, W. Chen, W. Sun, Z. Chen, J. Pei, D. He, C. Lv, D. Wang, Y. Li, Rational control of the selectivity of a ruthenium catalyst for hydrogenation of 4-Nitro-styrene by strain regulation, *Angew. Chem. Int. Ed.* 56 (2017) 11971–11975.
- [33] L. Li, G. Chen, H. Zheng, W. Meng, S. Jia, L. Zhao, P. Zhao, Y. Zhang, S. Huang, T. Huang, J. Wang, Room-temperature oxygen vacancy migration induced reversible phase transformation during the anelastic deformation in CuO, *Nat. Commun.* 12 (2021) 3863.
- [34] W. Zhu, X. Chen, J. Jin, X. Di, C. Liang, Z. Liu, Insight into catalytic properties of Co<sub>3</sub>O<sub>4</sub>-CeO<sub>2</sub> binary oxides for propane total oxidation, *Chinese, J. Catal.* 41 (2020) 679–690.
- [35] F. Jiang, S. Wang, B. Liu, J. Liu, L. Wang, Y. Xiao, Y. Xu, X. Liu, Insights into the influence of CeO<sub>2</sub> crystal facet on CO<sub>2</sub> hydrogenation to methanol over Pd/CeO<sub>2</sub> catalysts, *ACS Catal.* 10 (2020) 11493–11509.
- [36] B. Cui, L. Zhou, K. Li, Y. Q. Liu, D. Wang, Y. Ye, S. Li, Holey Co-Ce oxide nanosheets as a highly efficient catalyst for diesel soot combustion, *Appl. Catal. B-Environ.* 267 (2020), 118670.
- [37] B. Murugan, A.V. Ramaswamy, Defect-site promoted surface reorganization in nanocrystalline ceria for the low-temperature activation of ethylbenzene, *J. Am. Chem. Soc.* 129 (2007) 3062–3063.
- [38] X. Mao, S. Liu, W. Liu, X. Wu, S. Liu, A simple model catalyst study to distinguish the roles of different oxygen species in propane and soot combustion, *Appl. Catal. B-Environ.* 310 (2022), 121331.
- [39] Y.F. Sun, J.J. Li, F. Xie, Y. Wei, M. Yang, Ruthenium-loaded cerium dioxide nanocomposites with rich oxygen vacancies promoted the highly sensitive electrochemical detection of Hg(II), *Sens. Actuat. B-Chem.* 320 (2020), 128355.
- [40] H. Li, J. Shang, Z. Ai, L. Zhang, Efficient visible light nitrogen fixation with BiOBr nanosheets of oxygen vacancies on the exposed {001} facets, *J. Am. Chem. Soc.* 137 (2015) 6393–6399.
- [41] A. Filtschew, K. Hofmann, C. Hess, Ceria and its defect structure: New insights from a combined spectroscopic approach, *J. Phys. Chem. C* 120 (2016) 6694–6703.
- [42] S. Mo, S. Li, Q. Ren, M. Zhang, Y. Sun, B. Wang, Z. Feng, Q. Zhang, Y. Chen, D. Ye, Vertically-aligned Co<sub>3</sub>O<sub>4</sub> arrays on Ni foam as monolithic structured catalysts for CO oxidation: effects of morphological transformation, *Nanoscale* 10 (2018) 7746–7758.
- [43] Y. Li, W. Han, R. Wang, L.T. Weng, A. Serrano-Lotina, M.A. Bañares, Q. Wang, K. L. Yeung, Performance of an aliovalent-substituted CoCeO<sub>x</sub> catalyst from bimetallic MOF for VOC oxidation in air, *Appl. Catal. B-Environ.* 275 (2020), 119121.
- [44] L. Liu, Y. Chen, L. Dong, J. Zhu, H. Wan, B. Liu, B. Zhao, H. Zhu, K. Sun, L. Dong, Y. Chen, Investigation of the NO removal by CO on CuO-CoO<sub>x</sub> binary metal oxides supported on Ce<sub>0.67</sub>Zr<sub>0.33</sub>O<sub>2</sub>, *Appl. Catal. B-Environ.* 90 (2009) 105–114.
- [45] D. Chen, J. Zhong, W. Chu, Z. Wu, A. Kuzmin, N. Mironova-Ulmane, A. Marcelli, Structural disorder and electronic hybridization in Ni<sub>2</sub>Mg<sub>1-x</sub>O solid solutions probed by XANES at the oxygen K edge, *J. Phys. -Condens. Mat.* 19 (2007), 356219.
- [46] J.S. Lee, Y.W. Xie, H.K. Sato, C. Bell, Y. Hikita, H.Y. Hwang, C.C. Kao, Titanium dxy ferromagnetism at the LaAlO<sub>3</sub>/SrTiO<sub>3</sub> interface, *Nat. Mater.* 12 (2013) 703–706.
- [47] C. Song, Q. Zhan, F. Liu, C. Wang, H. Li, X. Wang, X. Guo, Y. Cheng, W. Sun, L. Wang, J. Qian, B. Pan, Overturned loading of inert CeO<sub>2</sub> to active Co<sub>3</sub>O<sub>4</sub> for unusually improved catalytic activity in fenton-like reactions, *Angew. Chem. Int. Ed.* 61 (2022), e202200406.
- [48] L. Cheng, X. Yue, J. Fan, Q. Xiang, Site-specific electron-driving observations of CO<sub>2</sub>-to-CH<sub>4</sub> photoreduction on Co-doped CeO<sub>2</sub>/crystalline carbon nitride S-scheme heterojunctions, *Adv. Mater.* (2022), e2200929.
- [49] J. Luo, M. Meng, X. Li, X. Li, Y. Zha, T. Hu, Y. Xie, J. Zhang, Mesoporous Co<sub>3</sub>O<sub>4</sub>-CeO<sub>2</sub> and Pd/Co<sub>3</sub>O<sub>4</sub>-CeO<sub>2</sub> catalysts: Synthesis, characterization and mechanistic study of their catalytic properties for low-temperature CO oxidation, *J. Catal.* 254 (2008) 310–324.
- [50] F. Giannici, G. Gregori, C. Aliotta, A. Longo, J. Maier, A. Martorana, Structure and oxide ion conductivity: local order, defect interactions and grain boundary effects in acceptor-doped ceria, *Chem. Mater.* 26 (2014) 5994–6006.
- [51] C. Zhang, A. Acharya, On the relevance of generalized disclinations in defect mechanics, *J. Mech. Phys. Solids* 119 (2018) 188–223.
- [52] D. Lee, X. Gao, L. Sun, Y. Jee, J. Poplawsky, T.O. Farmer, L. Fan, E.J. Guo, Q. Lu, W. T. Heller, Y. Choi, D. Haskel, M.R. Fitzsimmons, M.F. Chisholm, K. Huang, B. Yildiz, H.N. Lee, Colossal oxygen vacancy formation at a fluorite-bixbyite interface, *Nat. Commun.* 11 (2020) 1371.
- [53] A. Orera, F. Wang, E. Ferreira-Vila, S. Serrano-Zabaleta, A. Larrañaga, M. A. Laguna-Bercero, E.C. Dickey, F. Rivadulla, M.C. Muñoz, Á. Larrea, Interfacial stability and ionic conductivity enhanced by dopant segregation in eutectic ceramics: the role of Gd segregation in doped CeO<sub>2</sub>/CoO and CeO<sub>2</sub>/NiO interfaces, *J. Mater. Chem. A* 8 (2020) 2591–2601.
- [54] Y. Lu, Y. Huang, Y. Zhang, J.-J. Cao, H. Li, C. Bian, S.C. Lee, Oxygen vacancy engineering of Bi<sub>2</sub>O<sub>3</sub>/Bi<sub>2</sub>O<sub>2</sub>CO<sub>3</sub> heterojunctions: implications of the interfacial charge transfer, NO adsorption and removal, *Appl. Catal. B-Environ.* 231 (2018) 357–367.
- [55] W. Li, L. Zhao, C. Wang, X. Lu, W. Chen, Interface engineering of heterogeneous CeO<sub>2</sub>-CoO nanofibers with rich oxygen vacancies for enhanced electrocatalytic oxygen evolution performance, *ACS Appl. Mater. Inter.* 13 (2021) 46998–47009.
- [56] J. Ji, M. Jing, X. Wang, W. Tan, K. Guo, L. Li, X. Wang, W. Song, L. Cheng, J. Sun, W. Song, C. Tang, J. Liu, L. Dong, Activating low-temperature NH<sub>3</sub>-SCR catalyst by breaking the strong interface between acid and redox sites: A case of model Ce<sub>2</sub>(SO<sub>4</sub>)<sub>3</sub>-CeO<sub>2</sub> study, *J. Catal.* 399 (2021) 212–223.
- [57] L. Wang, X. Cheng, Z. Wang, C. Ma, Y. Qin, Investigation on Fe-Co binary metal oxides supported on activated semi-coke for NO reduction by CO, *Appl. Catal. B-Environ.* 201 (2017) 636–651.
- [58] H. Liu, L. Liu, L. Wei, B. Chu, Z. Qin, G. Jin, Z. Tong, L. Dong, B. Li, Preparation of three-dimensionally ordered macroporous MFe<sub>2</sub>O<sub>4</sub> (M = Co, Ni, Cu) spinel catalyst and its simultaneous catalytic application in CO oxidation and NO + CO reaction, *Fuel* 272 (2020), 117738.
- [59] G. Cheng, Z. Cai, X. Song, X. Chen, W. Dai, X. Fu, Visible light enhanced thermocatalytic CO + NO reaction over metastable NiCo<sub>2</sub>O<sub>4</sub> catalyst, *Appl. Catal. B-Environ.* 304 (2022), 120988.
- [60] P. Savva, A. Efstathiou, The influence of reaction temperature on the chemical structure and surface concentration of active NO<sub>x</sub> in H<sub>2</sub>-SCR over Pt/MgO/CeO<sub>2</sub>: SSITKA-DRIFTS and transient mass spectrometry studies, *J. Catal.* 257 (2008) 324–333.
- [61] A.M. Efstathiou, Elucidation of mechanistic and kinetic aspects of water-gas shift reaction on supported Pt and Au catalysts via transient isotopic techniques, *Catalysis* 28 (2016) 175–236.
- [62] Y. Zhang, L. Zhao, M. Kang, Z. Chen, S. Gao, H. Hao, Insights into high CO-SCR performance of CuCoAlO catalysts derived from LDH/MOFs composites and study of H<sub>2</sub>O/SO<sub>2</sub> and alkali metal resistance, *Chem. Eng. J.* 426 (2021), 131873.